JGP Journal of General Physiology

COMMUNICATION

Gating and anion selectivity are reciprocally regulated in TMEM16A (ANO1)

José J. De Jesús-Pérez[1], Ana E. López-Romero[1], Odalys Posadas[1], Guadalupe Segura-Covarrubias[1], Iván Aréchiga-Figueroa[2], Braulio Gutiérrez-Medina[3], Patricia Pérez-Cornejo[4], and Jorge Arreola[1]

Numerous essential physiological processes depend on the TMEM16A-mediated Ca^{2+}-activated chloride fluxes. Extensive structure–function studies have helped to elucidate the Ca^{2+} gating mechanism of TMEM16A, revealing a Ca^{2+}-sensing element close to the anion pore that alters conduction. However, substrate selection and the substrate–gating relationship in TMEM16A remain less explored. Here, we study the gating–permeant anion relationship on mouse TMEM16A expressed in HEK 293 cells using electrophysiological recordings coupled with site-directed mutagenesis. We show that the apparent Ca^{2+} sensitivity of TMEM16A increased with highly permeant anions and SCN^- mole fractions, likely by stabilizing bound Ca^{2+}. Conversely, mutations at crucial gating elements, including the Ca^{2+}-binding site 1, the transmembrane helix 6 (TM6), and the hydrophobic gate, impaired the anion permeability and selectivity of TMEM16A. Finally, we found that, unlike anion-selective wild-type channels, the voltage dependence of unselective TMEM16A mutant channels was less sensitive to SCN^-. Therefore, our work identifies structural determinants of selectivity at the Ca^{2+} site, TM6, and hydrophobic gate and reveals a reciprocal regulation of gating and selectivity. We suggest that this regulation is essential to set ionic selectivity and the Ca^{2+} and voltage sensitivities in TMEM16A.

Introduction

A variety of essential physiological functions, including blood pressure, electrolyte and hormone secretion, gastrointestinal rhythmicity, pain, neuronal and muscle excitability, and olfactory transduction, depend on the activation of Ca^{2+}-dependent chloride (Cl^-) channels TMEM16A and TMEM16B (Hartzell et al., 2005; Duran et al., 2010; Berg et al., 2012; Pedemonte and Galietta, 2014). Both channels are homodimer proteins harboring an independent anion permeation pathway in each monomer (Paulino et al., 2017; Dang et al., 2017; Sheridan et al., 2011). TMEM16A and TMEM16B are gated by the direct, voltage-dependent binding of intracellular Ca^{2+} ions to high-affinity binding sites (Arreola et al., 1996; Xiao et al., 2011; Contreras-Vite et al., 2016; Qu and Hartzell, 2000; Terashima et al., 2013). Three Ca^{2+} binding sites (sites 1–3) have been projected in each subunit (Yu et al., 2012; Tien et al., 2014; Le and Yang, 2020). Among them, site 1 is the best characterized both structurally and functionally. It is formed by four glutamates from transmembrane helices (TM) 6, 7, and 8, one aspartate from TM8, and one asparagine from TM6, which together coordinate the binding of two Ca^{2+} ions (Paulino et al., 2017; Dang et al., 2017).

Fig. 1, based on the Ca^{2+}-bound structure of TMEM16A PDB accession no. 5OYB (Paulino et al., 2017), shows the TM3–TM8 (gray ribbons) surrounding the pore (teal mesh) in a single subunit. Site 1 locates toward the cytoplasmic side, near a wide water-filled cavity accessible to the cytoplasm where it faces the permeation pathway. Site 2 has a low affinity for Ca^{2+} (within the micromolar range) and is occupied by this cation in a voltage-independent manner (Jeng et al., 2016; Lim et al., 2016). A third Ca^{2+} binding site is formed by one glutamate and one lysine on the TM2 and two aspartates on the TM10 (Le and Yang, 2020). Interestingly, it has been suggested that site 3 can allosterically regulate site 1 (Le and Yang, 2020).

The pore is formed by two large vestibules located at the entrances connected by a narrow neck, thinner than the

[1]Physics Institute, Universidad Autónoma de San Luis Potosí, San Luis Potosí, México; [2]Consejo Nacional de Ciencia y Tecnología, Facultad de Medicina, Universidad Autónoma de San Luis Potosí, San Luis Potosí, México; [3]Advanced Materials Division, Instituto Potosino de Investigación Científica y Tecnológica, San Luis Potosí, México; [4]Department of Physiology and Biophysics, Facultad de Medicina, Universidad Autónoma de San Luis Potosí, San Luis Potosí, México.

Correspondence to Jorge Arreola: arreola@dec1.ifisica.uaslp.mx

J.J. De Jesús-Pérez's current address is Department of Systems Pharmacology and Translational Therapeutics, University of Pennsylvania, Perelman School of Medicine, Philadelphia, PA. G. Segura-Covarrubias's current address is Department of Physiology and Biophysics, Case Western Reserve University, Cleveland, OH.

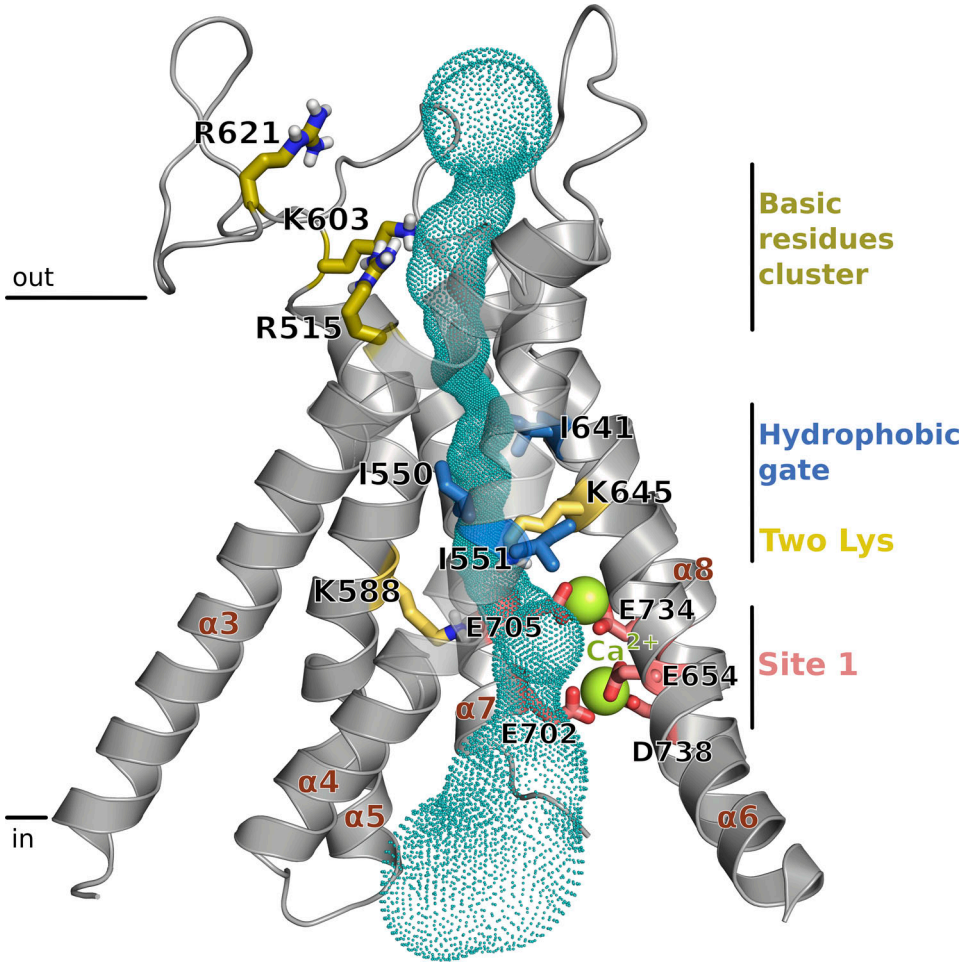

Figure 1. **The anion permeation pathway of TMEM16A with the high-affinity Ca^{2+} binding site occupied.** One subunit of TMEM16A with its extracellular (top) and intracellular (bottom) sides is shown. The anion permeation pathway is drawn as a teal mesh, and the α-helices 3–8 surrounding the pore are shown in gray. The green spheres are two Ca^{2+} ions sitting in the Ca^{2+} pocket of site 1. Note that residues of the hydrophobic gate (I641) and Ca^{2+} pocket (N650 and E654) are part of TM6. Thus, when Ca^{2+} binding occurs, the translational movement of TM6 is outwardly transmitted to open the hydrophobic gate. The side chains of the extracellular cluster of basic residues (olive), the hydrophobic gate (blue), two lysines at the middle of the pore (yellow), and the Ca^{2+} pocket of site 1 (orange) involved in anion selectivity were modeled as sticks.

hydrated Cl^- ion size (Fig. 1). At the narrow neck region, an inner hydrophobic gate formed by a triad of isoleucine residues (I641, I550, and I551 in TMEM16A ac) maintains the pore closed (Lam et al., 2021). In addition, the apo Ca^{2+} pocket of site 1 generates a strong negative electrostatic potential known as the electrostatic gate that hampers anion conductance (Lam and Dutzler, 2018). When the intracellular Ca^{2+} increases, the site 1 electrostatic potential and depolarizing voltages assist Ca^{2+} binding to site 1 (Fig. 1). The immediate consequence of Ca^{2+} binding is the plummeting of the electrostatic barrier, also referred to as "electrostatic gate opening." A subsequent effect of Ca^{2+} binding is the hinge movement of the cytosolic half of TM6 around glycine 644 (G644). The move of TM6 marks the opening of the steric hydrophobic gate. Thus, the concerted action of electrostatic and steric gating triggered by Ca^{2+} binding is required to open the pore and enable Cl^- permeation (Lam and Dutzler, 2018; Paulino et al., 2017). Additionally, upon disruption of the hydrophobic gate or the hinge movement of TM6 by mutation, the voltage can induce Cl^- permeation without intracellular Ca^{2+} (Lam et al., 2021).

The juxtaposition of the anion permeation pathway and site 1 would induce an interaction of the permeant anion with the gating elements that may influence Ca^{2+} binding, a critical step for TMEM16A activation. In agreement, early observations have shown that anions more permeable than Cl^- accelerate the onset and slow the offset of the Ca^{2+}-activated Cl^- currents in rat parotid acinar cells, thus affecting the voltage dependence of endogenous TMEM16A (Perez-Cornejo et al., 2004; Xiao et al., 2011). In TMEM16B, such anions aided the voltage dependency and increased the apparent Ca^{2+} sensitivity (Betto et al., 2014). Furthermore, applying thiocyanate to the cytoplasmic side of membrane patches excised from *Xenopus laevis* oocytes increased the apparent Ca^{2+} sensitivity of the endogenous TMEM16A (Wozniak et al., 2018; Qu and Hartzell, 2000). Thus, permeant anions interact with TMEM16A gating. However, during molecular interactions, the charge distribution of each participant is affected by the presence of others (Murray and Politzer, 2017). Therefore, the gating elements may be expected to affect anion permeation. In agreement, structural studies of TMEM16A

revealed that Cl^- ions pass in front of site 1 during permeation, and site 1 alters the channel's anion conductivity by generating a negative electrostatic potential (Fig. 1; Lam and Dutzler, 2018). Together, these observations suggested that permeant anions and the gating machinery of TMEM16 interact reciprocally. This idea implies that permeant anions affect Ca^{2+} and voltage sensitivities, key gating properties, whereas the gating elements alter permeability and anion selectivity.

Here, we used inside-out patches and whole-cell recordings to determine the effects of permeant anions on the apparent Ca^{2+} sensitivity and voltage dependence of WT TMEM16A. In addition, we applied site-directed mutagenesis to investigate whether the gating elements (site 1, TM6, and the steric hydrophobic gate) regulate anion permeability and selectivity. Our results indicate that the Ca^{2+} sensitivity is influenced by the presence of anions in the pore; conversely, the gating elements control anion selectivity. Furthermore, channels lost their anion selectivity and sensitivity to thiocyanate mole fractions (MFs) after we mutated key residues at several gating elements. We suggest that the activation and anion selectivity of TMEM16A depends on a reciprocal regulation of permeation and gating.

Materials and methods

Cell culture and channels expression

We used human embryonic kidney 293 (HEK 293) cells to express WT and mutant channels. HEK 293 cells were cultured in DMEM (Gibco) supplemented with 10% FBS and 0.1% gentamicin at 37°C in a 95% O_2/5% CO_2 atmosphere. WT mouse TMEM16A (ac) and mutant DNAs cloned in the pIRESII-EGFP vector (Clontech) were transfected (1 µg/µl cDNA) using the Polyfect transfection reagent (Qiagen), according to the manufacturer's instructions. Successfully transfected cells were used 12 h after transfection. Cells were seeded on coverslips at low density for whole-cell recording. Cells stably transfected with TMEM16A or transiently transfected with mutants were plated onto poly-L-lysine–coated coverslips for inside-out recordings. On the day of the experiment, we submerged one coverslip in a recording chamber flooded with the standard external solution and placed it on the stage of an inverted microscope (Nikon).

Mutagenesis

We introduced site-directed mutations using the Quick-change kit (Agilent) and verified them by sequencing.

Macroscopic current recordings

We recorded macroscopic currents at room temperature (21–23°C) from whole cells or inside-out patches using the patch-clamp technique as we previously reported (Cruz-Rangel et al., 2017). Cells expressing the channel of interest were selected by their GFP fluorescence using an inverted microscope (Nikon) equipped with UV illumination. We fabricated borosilicate patch pipettes using the P-97 electrode puller (Sutter Instruments). When filled with the standard pipette solution, the pipette resistances were 3–5 MΩ for the whole cell or 1–2 MΩ for inside-out patches. Currents from inside-out patches held at +80 mV were induced by rapid application to the cytosolic side of solutions containing increasing $[Ca^{2+}]$. The stimulation protocol for whole-cell recordings consisted of voltage steps from −100 to +200 mV delivered every 7 s from a holding potential of −30 mV, followed by a repolarization potential to −100 mV. Alternatively, we recorded whole-cell currents using a ramp protocol that varied the membrane potential between −80 and +80 mV. Data were acquired using an Axon Digidata 1550, an Axopatch 200B amplifier, and the pClamp10 software (Molecular Devices). Currents were filtered at 5 kHz and digitized at 10 kHz. For inside-out recordings using patch pipettes filled with solutions containing foreign anions, we embedded the Ag/AgCl recording electrode in a 1-M KCl agar guard. Recording chamber solutions were applied using a homemade gravity perfusion system and grounded using a 3-M KCl agar-bridge connected to an Ag/AgCl reference electrode.

Solutions to record macroscopic currents

We obtained all the recordings using extracellular solutions made hypertonic with D-mannitol, with their pH adjusted to 7.3 to inhibit the activation of endogenous volume-sensitive Cl^- and proton-activated channels (Hernández-Carballo et al., 2010; Ullrich et al., 2019). The standard extracellular solution contained (in mM) 139 TEA-Cl, 20 HEPES, 0.5 $CaCl_2$, and 110 D-mannitol. We adjusted the pH to 7.3 with TEAOH or NaOH. The solution's tonicity was 380–400 mOsm/kg measured by the vapor pressure point method with a VAPRO (Wescor). We replaced the Cl^- content in the standard extracellular solution with the desired foreign anion (SCN^-, I^-, NO_3^-, or Br^-) for anion selectivity sequence determination. External solutions with varying SCN^- MF were prepared by mixing the appropriate volumes of solutions containing 100% Cl^- and 100% SCN^-. The total anion concentration of the external solutions was 140 mM. The intracellular solutions with different $[Ca^{2+}]$ contained (in mM) 35.1 TEA-Cl, 25 EGTA-TEA, and 2.43 $CaCl_2$, for $[Ca^{2+}]_i$ = 0.1 µM; 30 TEA-Cl, 25 EGTA-TEA, and 5.24 $CaCl_2$ for $[Ca^{2+}]_i$ = 0.2 µM; 30 TEA-Cl, 25.24 EGTA-TEA, and 5.24 $CaCl_2$ for $[Ca^{2+}]_i$ = 0.25 µM; 22.48 TEA-Cl, 25 EGTA-TEA, and 8.76 $CaCl_2$ for $[Ca^{2+}]_i$ = 0.5 µM; 27.4 TEA-Cl, 25 HEDTA-TEA, and 6.3 $CaCl_2$ for $[Ca^{2+}]_i$ = 1.3 µM; 11.8 TEA-Cl, 25 HEDTA-TEA, and 14.1 $CaCl_2$ for $[Ca^{2+}]_i$ = 5 µM; and 2 TEA-Cl, 25 HEDTA-TEA, and 19 $CaCl_2$ for $[Ca^{2+}]_i$ = 12 µM. In addition, these solutions contained 50 mM HEPES and 85 mM D-mannitol. We adjusted the pH to 7.3 with TEA-OH and the tonicity to 290–300 mOsm/kg. The free $[Ca^{2+}]$ was calculated using Maxchelator (https://somapp.ucdmc.ucdavis.edu/pharmacology/bers/maxchelator/). The standard intracellular solution contained $[Ca^{2+}]_i$ = 0.2 µM. The $[Cl^-]$ in these solutions was 40 mM. All chemicals were purchased from Sigma-Aldrich or Merck.

Electrostatic potential profiles calculations

The apo (PDB accession no. 5OYG) and holo (PDB accession no. 5OYB) structures of mouse TMEM16A isoform ac (Paulino et al., 2017) were embedded in a POPC (1-palmitoyl-2-oleoyl-sn-glycero-3-phosphocholine) membrane and solvated with 140 mM NaCl. These ensembles were then equilibrated for 30 ns using Gromacs 5.1. I-tasser (https://zhanglab.ccmb.med.umich.edu/I-TASSER/) was used to model the protein gaps. By solving the linearized Poisson–Boltzmann equation in CHARMM-GUI PBED

solver, the average electrostatic potential along the pore was calculated on a 255 × 197 × 273-Å^3 (0.5-Å grid spacing), with CHARMM36 forcefield. We generated the in silico mutants with CHARMM-GUI tools. The pore in the structure was located using CAVER 3.0 (https://caver.cz/index.php?sid=100) and visualized with PyMol. We calculated the average electrostatic potential on the transversal area determined by the pore radius. For this calculation, the thickness of the membrane was 35 Å. The dielectric constants were set to 2 for the protein, 2 for the membrane, 30 for the membrane headgroups, and 80 for solvent containing 140 mM salt concentration (Jo et al., 2008a; Im et al., 1998; Jo et al., 2008b; Lam and Dutzler, 2018).

Data analysis

Data were analyzed and plotted using pClamp 10 (Molecular Devices) and Origin 9 (Origin Lab). The concentration–response curves to Ca^{2+} were constructed by plotting the current magnitude induced by a given $[Ca^{2+}]_i$ and then fitting with the Hill equation (Eq. 1) to obtain the $[Ca^{2+}]_i$ needed to get 50% of the response (EC_{50}) and the Hill coefficient (n_H):

$$Response = \frac{(I_{max} - I_{min})}{1 + \left(\frac{EC_{50}}{[Ca^{2+}]_i}\right)^{n_H}}, \quad (1)$$

where I_{max} and I_{min} are the maximum and minimum responses, respectively. We analyzed the voltage dependence of WT and mutant TMEM16A channels activated in the presence of 0, 0.2, 0.5, and 12 µM Ca^{2+}. Because the channels did not reach a maximum conductance under these conditions, we calculated the parameters of the sigmoidal curves in the following manner. First, we converted each current–voltage (I-V) relationship to raw conductance–voltage (G-V) relationship. The raw conductance was calculated as $G = I / (V - Vr)$. Then, we fitted individual G-V plots to Eq. 2 to estimate an apparent G_{max} at a given $[Ca^{2+}]_i$ ($G_{max\_app,\ x\ \mu M\ Ca^{2+}}$). The resulting $G_{max\_app,\ x\ \mu M\ Ca^{2+}}$ was used to normalize G values obtained at the x µM Ca^{2+}. Finally, the $G/G_{max\_app,\ x\ \mu M\ Ca^{2+}}$ values at each V were averaged (± SEM), plotted against V, and fitted with Eq. 2.

$$\frac{G}{G_{max\_app,x\mu MCa^{2+}}} = \frac{1}{1 + e^{k(V - V_{0.5\_app})}}, \quad (2)$$

where $V_{0.5\_app}$ and k represent the voltage needed to reach the curve's midpoint and the slope, respectively. The reversal potential, Vr, was determined from the I-V relationship. We selected segments of the ramp-generated I-V curves or plotted the absolute current values generated by step voltages both around the reversal potential. I-V relationships were then fit with a 3-order polynomial. From the fits, we determine the zero-current potential values. In addition, we estimated the liquid junction potential generated by each extracellular/intracellular solution pair using the Clampex routine of pClamp. Then the zero-current potential values were corrected using the estimated liquid junction potential (Neher, 1992). Finally, the changes in zero-current potentials upon anion exchange were determined and used to calculate the anion permeability relative to Cl^- permeability or permeability ratios (P_X/P_{Cl}) using the Goldman–Hodgkin–Katz Equation (Eq. 3):

$$\frac{P_X}{P_{Cl}} = \frac{[Cl]_{o,i} exp^{\frac{(\Delta Vr)F}{RT}} - [Cl]_{o,f}}{[X]_{o,f}}, \quad (3)$$

where X is a test anion, ΔVr (= Vr in anion X – Vr in Cl^-) is the Vr shift induced by Cl^- replacement with a foreign anion X, and $[Cl]_{o,i}$, $[Cl]_{o,f}$, and $[X]_{o,f}$ are the extracellular concentrations of Cl^- and X^- before (i) and after (f) replacement.

Statistics

Pooled data are presented as mean ± SEM of n (number of independent experiments). We performed statistical analysis of mean values using OriginLab. Significant differences between means were determined using Student's t test or one-way ANOVA followed by Tukey's correction with P = 0.01 (indicated by ** in the figures).

Online supplemental material

Fig. S1 A shows the magnitude of the background currents recorded from HEK 293 cells transfected with an empty vector. Cells were bathed in Cl^-- (black) and SCN^--containing (blue) solutions. Fig. S1 B shows that 0.5 µM Ani9, a TMEM16A blocker, inhibited the ion currents through the 5Q mutant channel. Fig. S2 shows the relationship between P_X/P_{Cl} ratios and anion hydration energies in different channels. In the WT pore, the P_X/P_{Cl} ratios increase linearly (olive symbols and line) as the hydration energy decreases, a relationship that is lost in the mutant channels.

Results

Foreign anions regulate the apparent Ca^{2+} sensitivity and voltage dependence of TMEM16A

To establish whether foreign anions regulate the apparent Ca^{2+} sensitivity of WT TMEM16A, we determined the Ca^{2+} EC_{50} using recordings from inside-out patches held at +80 mV as previously reported in TMEM16B (Betto et al., 2014). First, we excised patches using a pipette filled with a solution containing Cl^-, SCN^-, F^-, or NO_3^-, and exposed the cytosolic side to increasing $[Ca^{2+}]_i$. Fig. 2 A shows examples of the macroscopic currents induced by the indicated $[Ca^{2+}]_i$ while the extracellular side of the membrane patch was exposed to Cl^- (black), SCN^- (blue), F^- (green), or NO_3^- (red). As the $[Ca^{2+}]_i$ increased, the magnitude of the current flowing through WT channels increased until it saturated at 5–12 µM regardless of the external anion. Fig. 2 B shows the resulting dose–response curves to $[Ca^{2+}]_i$; the curves for SCN^- (blue) and NO_3^- (red) are shifted toward lower $[Ca^{2+}]$ values compared with the curves for Cl^- (black) and F^- (green) that are on higher $[Ca^{2+}]$ values. The curves were analyzed using Eq. 1 (continuous lines in Fig. 2 B) to obtain the EC_{50} and n_H coefficient values. Next, we plotted these parameters in Fig. 2 C as a function of the permeability ratio for the tested anion. As the permeability ratio increased, the EC_{50} value (black) decreased from 0.75 µM in the presence of F^- to 0.3 µM in SCN^-, whereas the Hill coefficient stayed 2.5–3 (light blue).

As more than one permeant anion can simultaneously be present in the TMEM16A pore, the zero-current potential and the anion conductance can display anomalous mole fraction

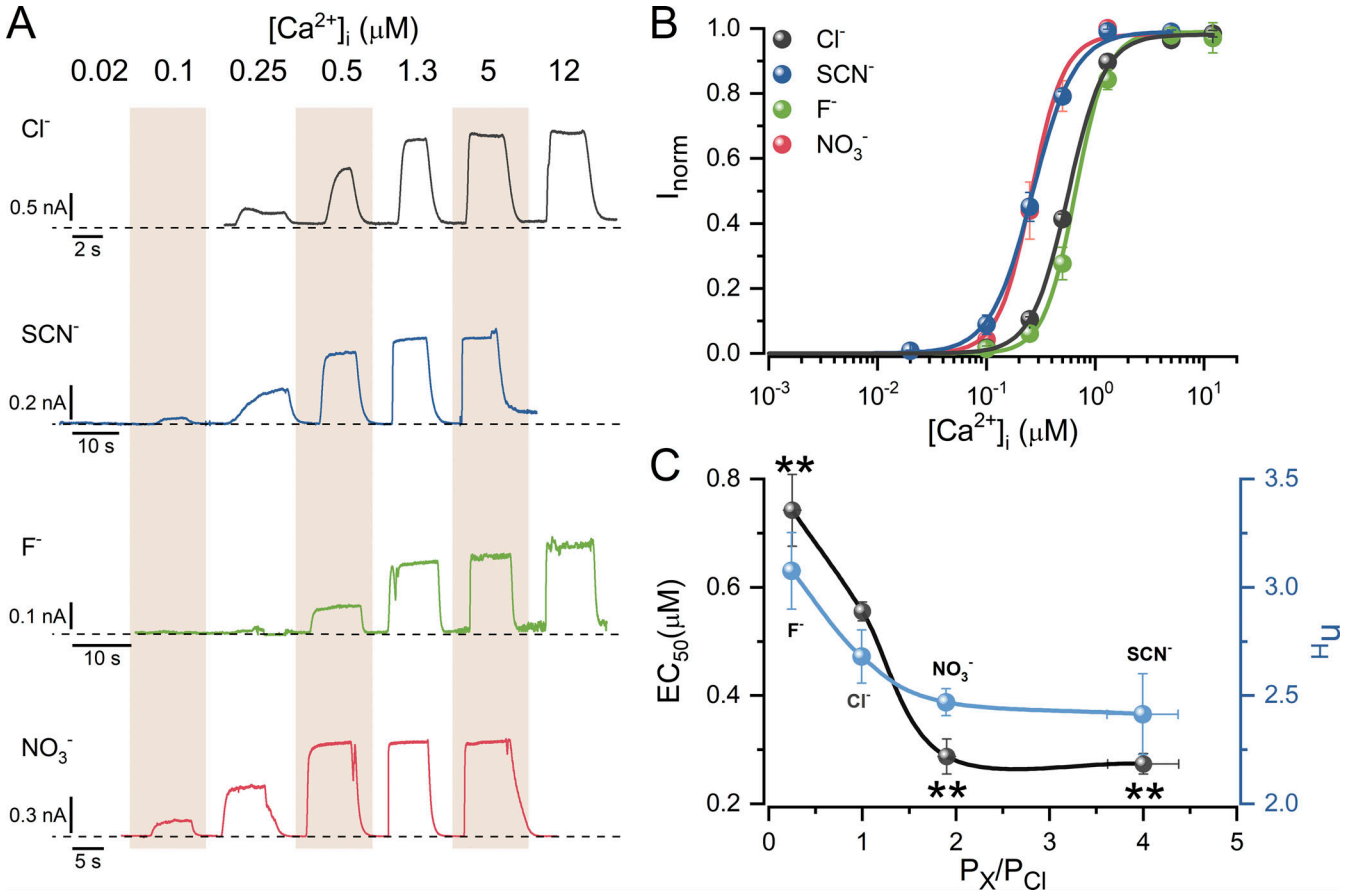

Figure 2. **Highly permeable anions enhance the apparent Ca^{2+} sensitivity in WT TMEM16A. (A)** Macroscopic currents induced by application of increasing $[Ca^{2+}]_i$ (indicated at the top of the recordings) to the cytosolic side of inside-out patches held at +80 mV. The extracellular side of the patches was exposed to a solution containing 140 mM of Cl^- (black, n = 7), SCN^- (blue, n = 6), F^- (green, n = 6), or NO_3^- (red, n = 6). $[Cl^-]_i$ = 40 mM, pH_e = pH_i = 7.3. **(B)** Concentration–response curves constructed with the current magnitudes shown in A. We used Hill equation fits (continuous lines) to compute EC_{50} and n_H coefficient. **(C)** Relationship between the permeability ratios of foreign anions present on the extracellular side and the EC_{50} and n_H coefficient. Permeability ratios were calculated as described in the legend of Fig. 5. **, Ca^{2+} EC_{50} values are statistically different (P = 0.01) from the Ca^{2+} EC_{50} calculated in the presence of Cl^-. The data were analyzed using one-way ANOVA with a Tukey's post-hoc test.

(AMF) behavior (Qu and Hartzell, 2000; Xiao et al., 2011). We hypothesized that more than one permeating anion could influence the site 1 Ca^{2+} affinity during the permeation process. If so, the Ca^{2+} affinity would display AMF behavior because Ca^{2+} ligation also occurs within the pore. We tested this idea by determining the Ca^{2+} EC_{50} at different SCN^- MF on the extracellular side. We chose SCN^- because it is approximately fourfold more permeable than Cl^- and induced small currents at +80 mV in mock-transfected cells (Fig. S1 A, upper panel). Fig. 3 A shows Ca^{2+}-induced macroscopic currents recorded from four independent inside-out patches excised with a pipette containing 0.25 (olive), 0.5 (orange), 0.75 (green), or 1 (blue) SCN^- MF. The $[Ca^{2+}]_i$ used to activate the currents are indicated at the top of the records. Fig. 3 B shows the resulting dose–response curves to Ca^{2+} under different external SCN^- MF. Compared with the 0 SCN^- MF condition, the curves shifted to lower $[Ca^{2+}]$ values as the SCN^- MF increased to 0.75. However, the curve with SCN^- MF of 1 was similar to that obtained with 0.5 MF. The EC_{50} and n_H parameters were calculated by fitting the dose–response curves to the Hill equation (continuous lines in Fig. 3 B). The calculated parameters are plotted as a function of the SCN^- MF in Fig. 3 C (black). The EC_{50} decreased as the SCN^- MF increased, reaching a minimum value when the SCN^- MF was 0.75. In contrast, the Hill coefficient remained constant at ~2.5. Although at +80 mV, the TMEM16A EC_{50} did not show a typical AMF behavior, at +100 mV (Fig. 3 C, gray symbols), we saw a minimum of ~0.5 and 0.75, indicative of abnormal behavior of Ca^{2+} sensitivity.

Given that the rates of association and dissociation of Ca^{2+} determine the apparent Ca^{2+} sensitivity, a property increased by highly permeant anions, we expected to see changes in on- or off-rates of the Ca^{2+}-induced currents in the presence of different anions or SCN^- MF. As we reported previously, it is possible to estimate these rates from inside-out patch recordings (Xiao et al., 2011). We calculated the apparent binding and unbinding rates of Ca^{2+} by fitting a single exponential function to the activation and deactivation segments of the TMEM16A current elicited by 5 μM Ca^{2+} applied to patches held at +80 mV. This $[Ca^{2+}]$ is ~10-fold the Ca^{2+} EC_{50} (Fig. 2 B); therefore, changes in the Ca^{2+} sensitivity would be readily apparent.

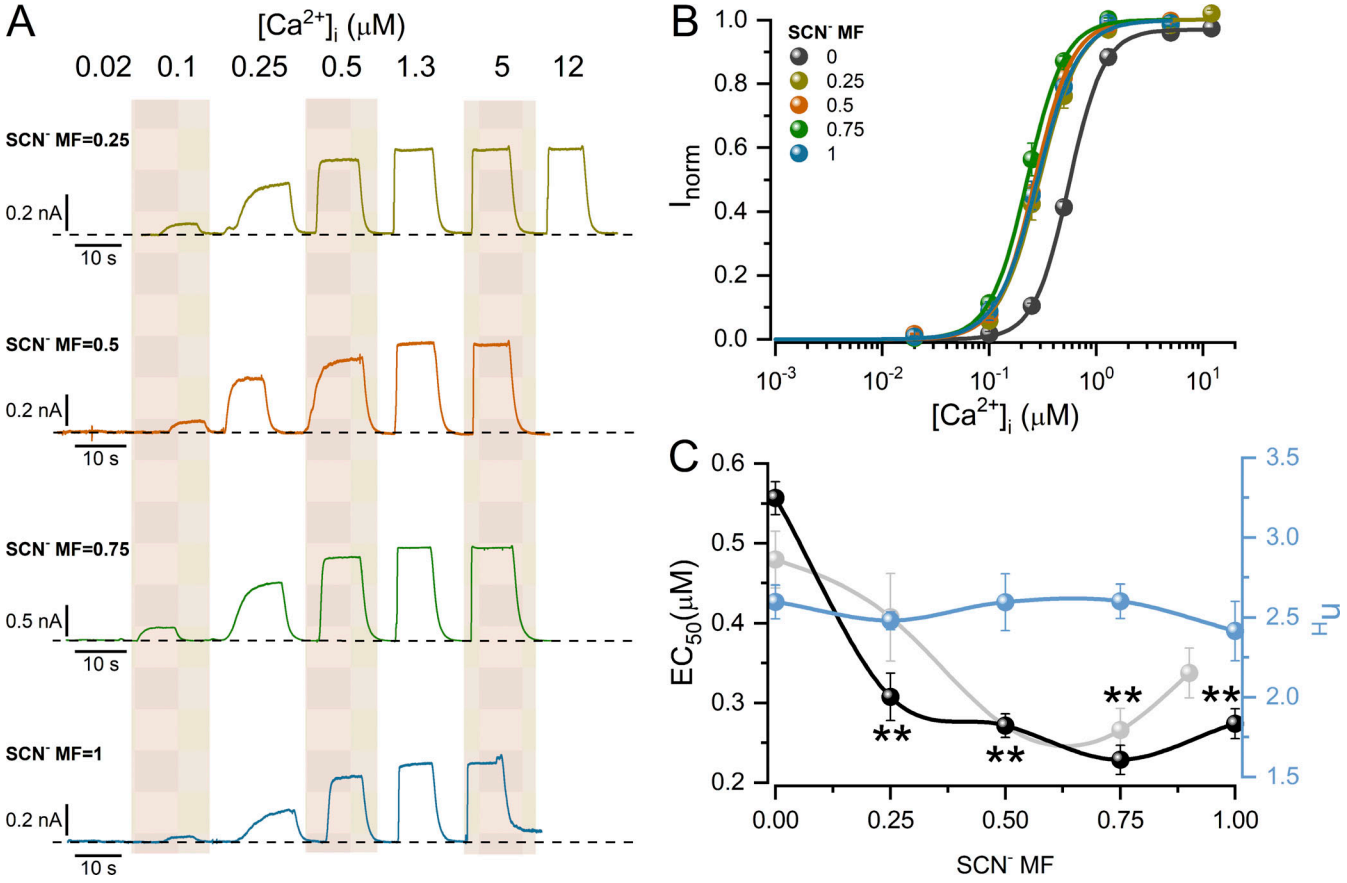

Figure 3. **SCN⁻ MFs induce AMF-like behavior on the apparent Ca^{2+} sensitivity of WT TMEM16A. (A)** Examples of macroscopic currents induced by applying increasing $[Ca^{2+}]_i$ (indicated at the top of the panel) to the cytosolic side of four different inside-out patches held at +80 mV. The extracellular side of the patches was exposed to 0.25 (olive, n = 9), 0.5 (orange, n = 7), 0.75 (green, n = 5), or 1 (blue, n = 6) SCN⁻ MF. $[Cl^-]_i$ = 40 mM, pH_e = pH_i = 7.3. **(B)** Concentration–response curves constructed with the current magnitudes obtained with 0, 0.25, 0.5, 0.75, and 1 SCN⁻ MF shown in A. Continuous lines are fits of Hill equation, used to determine EC_{50} and n_H coefficient. **(C)** Relationship between SCN⁻ MF present on the extracellular side of the patch and the EC_{50} (black) and n_H (blue) parameters. **, Ca^{2+} EC_{50} values are statistically different (P = 0.01) from the Ca^{2+} EC_{50} value calculated in 0 SCN⁻ MF. The data were analyzed using one-way ANOVA with a Tukey's post-hoc test. The gray curve shows the Ca^{2+} EC_{50} versus SCN⁻ MF at +100 mV (n > 7). n_H values were between 1.79 and 2.17.

Fig. 4 A shows examples of macroscopic currents recorded in the presence of F^-, Cl^-, NO_3^-, and SCN^- on the extracellular side. The red lines are the monoexponential fits to calculate τ_{on} and τ_{off}. With extracellular NO_3^- or SCN^-, the off-rate was slowed by 2.4- and 2.9-fold, respectively, without altering the on-rate (Fig. 4 A, right side). Similar recordings are shown in Fig. 4 B. In this case, we exposed the extracellular side to SCN^- MF = 0.25, 0.5, and 0.75. Increasing the SCN^- MF slowed down the off-rate nearly twofold without changing the on-rate (Fig. 4 B, right side). We obtained the same trend with data collected with 1.3 μM Ca^{2+}. On the right side, the average on and off time constant values are plotted as open circles in Fig. 4, A and B. These results further support the idea that permeant anions increase the apparent Ca^{2+} affinity of TMEM16A by slowing down the unbinding of Ca^{2+}. Thus, these data show that permeant anions probably regulate the apparent Ca^{2+} sensitivity of TMEM16A by stabilizing bound Ca^{2+}.

Provided that high $[Ca^{2+}]_i$ facilitates the voltage dependence of TMEM16A (Xiao et al., 2011) and the apparent Ca^{2+} affinity displayed AMF behavior with SCN^- MF, we anticipated alterations in the voltage dependence by the presence of anion MFs as previously demonstrated in CLC-0 and CLC-1 voltage-gated Cl^- channels (Pusch et al., 1995; Rychkov et al., 2001). We measured Cl^- currents from cells bathed in solutions containing different SCN^- MF to test this idea. Fig. 5 A shows an example of currents obtained in Cl^- (black) and SCN^- (red) recorded in the voltage range of −100 and +200 mV. The presence of SCN^- resulted in currents of greater magnitude and tail currents slower than those recorded in the presence of Cl^-. The $G/G_{max\_app,\ 0.5\ \mu M\ Ca^{2+}}$ calculated under different SCN^- MF was plotted as a function of voltage in Fig. 5 B. The curves seem to steadily shift to lower voltage values as the SCN^- MF increases. The total $V_{0.5\_app}$ shift was +83 mV (from +126 ± 7.8 mV with SCN^- MF = 0 to +43 ± 8 mV with SCN^- MF = 1). However, the $V_{0.5\_app}$ values show a nonlinear behavior (Fig. 5 C) with little or no change in the slope (Fig. 5 D). In addition, the reversal potential shifts plotted against the SCN^- MF (Fig. 5 E) cannot be explained by a constant P_{SCN}/P_{Cl} value (P_{SCN}/P_{Cl} = 4.7 in red and = 5.5 in blue). Instead, P_{SCN}/P_{Cl} varies as the SCN^- MF changes (Fig. 5 F). This behavior is compatible with AMF behavior, as previously reported (Qu and Hartzell, 2000; Xiao et al.,

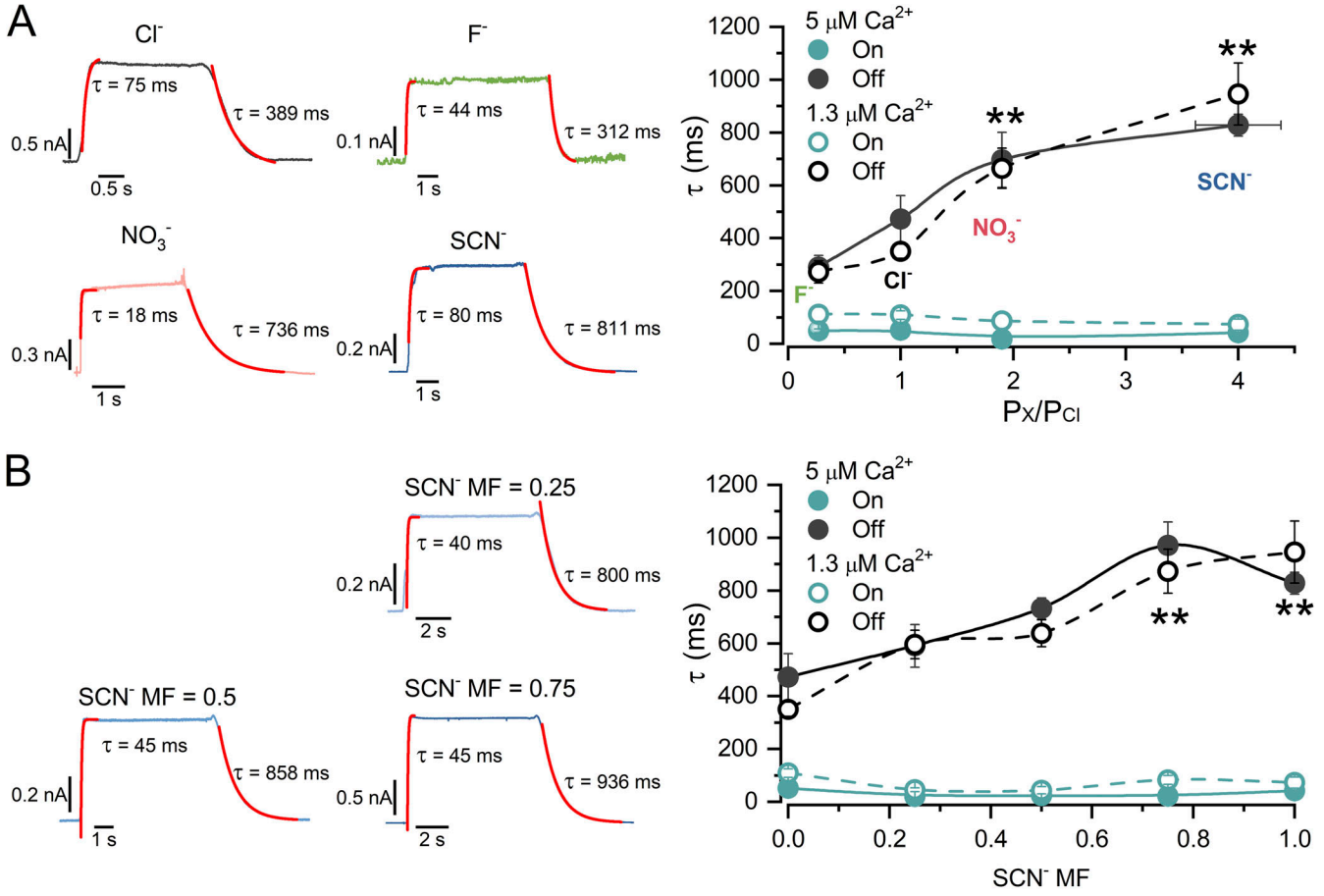

Figure 4. **The deactivation rate of WT TMEM16A currents slows down when highly permeant anions or solutions with increasing SCN^- MFs are present on the extracellular side. (A and B)** The activation and deactivation segments of the currents induced by application and removal of 5 μM $[Ca^{2+}]_i$, respectively, were fitted with a single exponential function (red lines) to determine their corresponding time constants τ_{on} and τ_{off}. The extracellular side of the patches was exposed to the indicated foreign anions (A) or increasing SCN^- MF (B). The plots on the right side summarize the effects of anions (upper) or SCN^- MF (bottom) on τ_{on} (black) and τ_{off} (aquamarine). Open symbols are τ_{on} and τ_{off} calculated from currents induced by 1.3 μM Ca^{2+}, and closed symbols are τ_{on} and τ_{off} calculated from currents induced by 5 μM Ca^{2+}. The total anion concentration on the extracellular side was 140 mM in all cases. Patches were held at +80 mV, $[Cl^-]_i$ = 40 mM, $pH_e = pH_i$ = 7.3. The number of independent experiments were 7 (Cl^-), 6 (SCN^-), 6 (F^-), 6 (NO_3^-), 9 (0.25), 7 (0.5), 5 (0.75), and 6 (1). **, τ_{off} values were statistically different (P = 0.01) from the τ_{off} calculated in the presence of F^- (A) and 0 SCN^- MF (B). The data were statistically analyzed using one-way ANOVA with a Tukey's post-hoc test.

2011). Thus, in addition to increasing the apparent Ca^{2+} affinity, SCN^- MF applied extracellularly strongly facilitated the TMEM16A voltage dependence.

The gating elements of TMEM16A take part in anion selectivity

Because the permeant anions stabilized the open conformation by decreasing the off-rate of Ca^{2+}-induced currents, which facilitates the gating process of CaCC (Perez-Cornejo et al., 2004), we anticipated that the gating machinery would reciprocally regulate anion selectivity. As described in the Introduction, the gating machinery of TMEM16A comprises electrostatic (acidic residues of site 1) and steric (TM6 and hydrophobic gate) elements. Therefore, we performed a mutagenesis analysis of these elements and determined the mutant channels' anion permeability and selectivity sequence to test further the idea of reciprocal regulation between permeation and gating.

To infer a possible role of site 1 in anion selection, we produced mutant TMEM16A channels E702Q, E705Q, E702Q/E705Q, and E654Q/E702Q/E705Q/E734Q/D738Q (5Q), determined their anion selectivity using whole-cell recordings, and compared it to WT TMEM16A channels recorded in the presence of 0.2 μM Ca^{2+}. These mutations decreased the Ca^{2+} affinity of site 1 (Tien et al., 2014; Yu et al., 2012); thus, we recorded them with 12 μM intracellular Ca^{2+}. Fig. 6 A displays I-V relations obtained from cells dialyzed with 0.2 mM Ca^{2+} that express WT channels (upper left) or with 12 μM Ca^{2+} that express E702Q (upper right), E705Q (middle left), and E702Q/E705Q (middle right) mutant channels. We bathed cells in 140 mM Cl^-, Br^-, NO_3^-, I^-, or SCN^- solutions and determined the reversal potential from the I-V relations under each ionic condition. We observed that currents increased with all foreign anions for the WT channel, and reversal potentials changed between −62 and −28 mV when external Cl^- was replaced by the indicated anions (Fig. 6 A, upper left). We used the changes of zero-current reversal potentials and the Goldman–Hodgkin–Katz Equation (Eq. 3) to calculate permeability ratios (P_X/P_{Cl}) and determine the

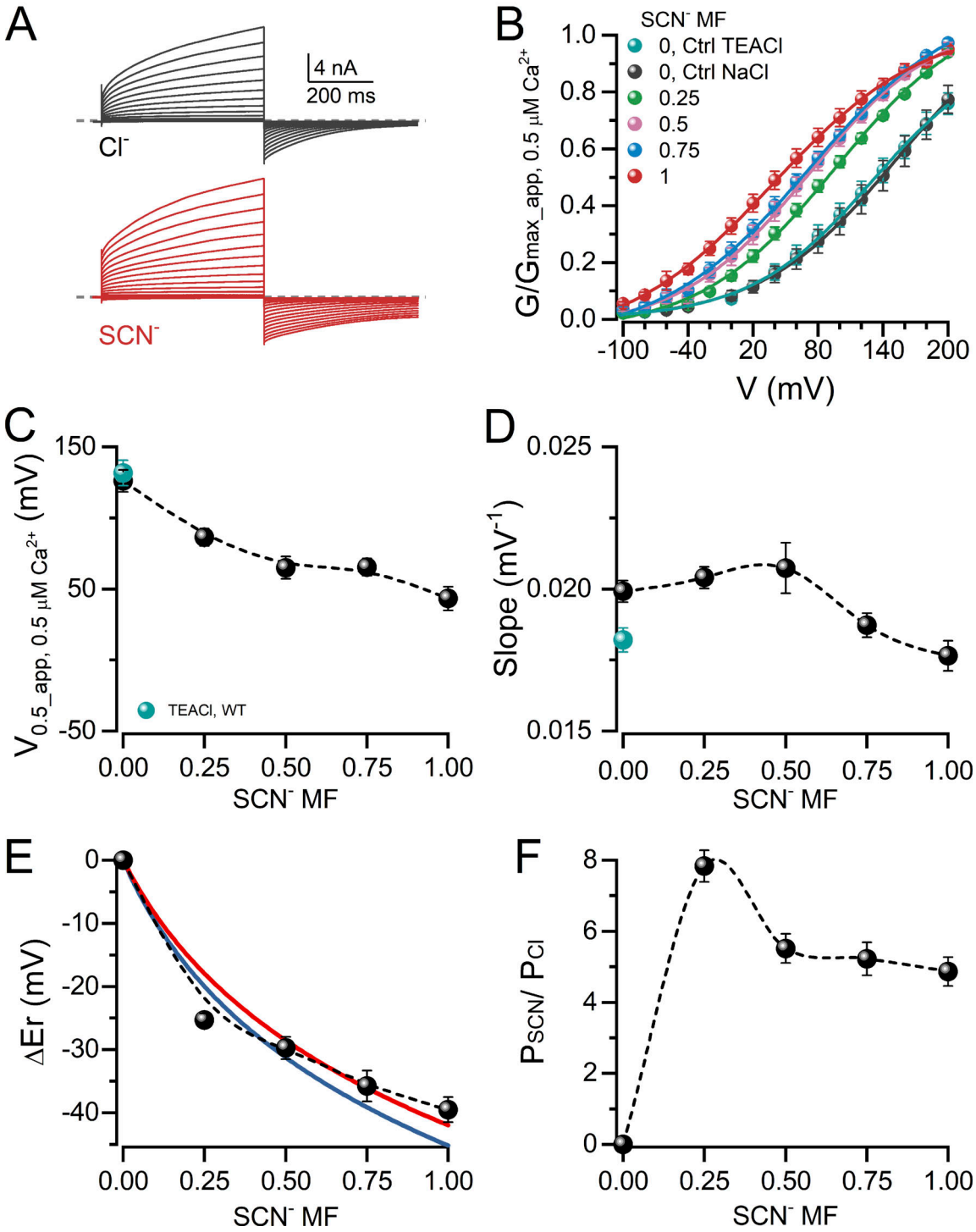

Figure 5. **SCN⁻ MFs facilitate the voltage dependence of activation and induce AMF-like behavior in WT TMEM16A. (A)** Pair of macroscopic currents recorded from a cell expressing the WT TMEM16A channel. The cell was dialyzed with 0.5 µM Ca^{2+} while bathed in a solution containing Cl^- (black) that was later replaced with SCN^- (red). Scale bars are valid for both sets of traces. Discontinuous blue lines indicate zero-current levels. **(B)** Voltage dependence of normalized conductance calculated as described in Materials and methods using the current magnitude of recordings like those shown in A, obtained in the presence of the indicated SCN^- MF (0.0, n = 8; 0.25, n = 7; 0.5, n = 8; 0.75, n = 7; 1.0, n = 10). Continuous lines are fits with the logistic Eq. 2 to determine $V_{0.5\_app}$ and slope values. **(C)** $V_{0.5\_app}$ at 0.5 µM Ca^{2+} and different SCN^- MF determined for WT channels. Values were obtained from fits shown in B. Note that the $V_{0.5\_app}$ value was the same in cells bathed in TEACl- or NaCl-containing solutions. **(D)** Slope values at different SCN^- MF determined for the WT channel. Values were obtained from fits shown in B. The aquamarine value was calculated from recordings obtained in TEACl. **(E)** Changes in current reversal potentials induced by replacing the external Cl^- with the indicated SCN^- MF. The currents were recorded from cells expressing the WT TMEM16A. The Goldman–Hodgkin–Katz equation simulated red and blue lines with P_{SCN}/P_{Cl} = 4.87 and 5.5, respectively. **(F)** P_{SCN}/P_{Cl} as a function of the SCN^- MF. Permeability ratios were calculated using the Goldman–Hodgkin–Katz equation (Eq. 3) and the changes of reversal potential shown in E.

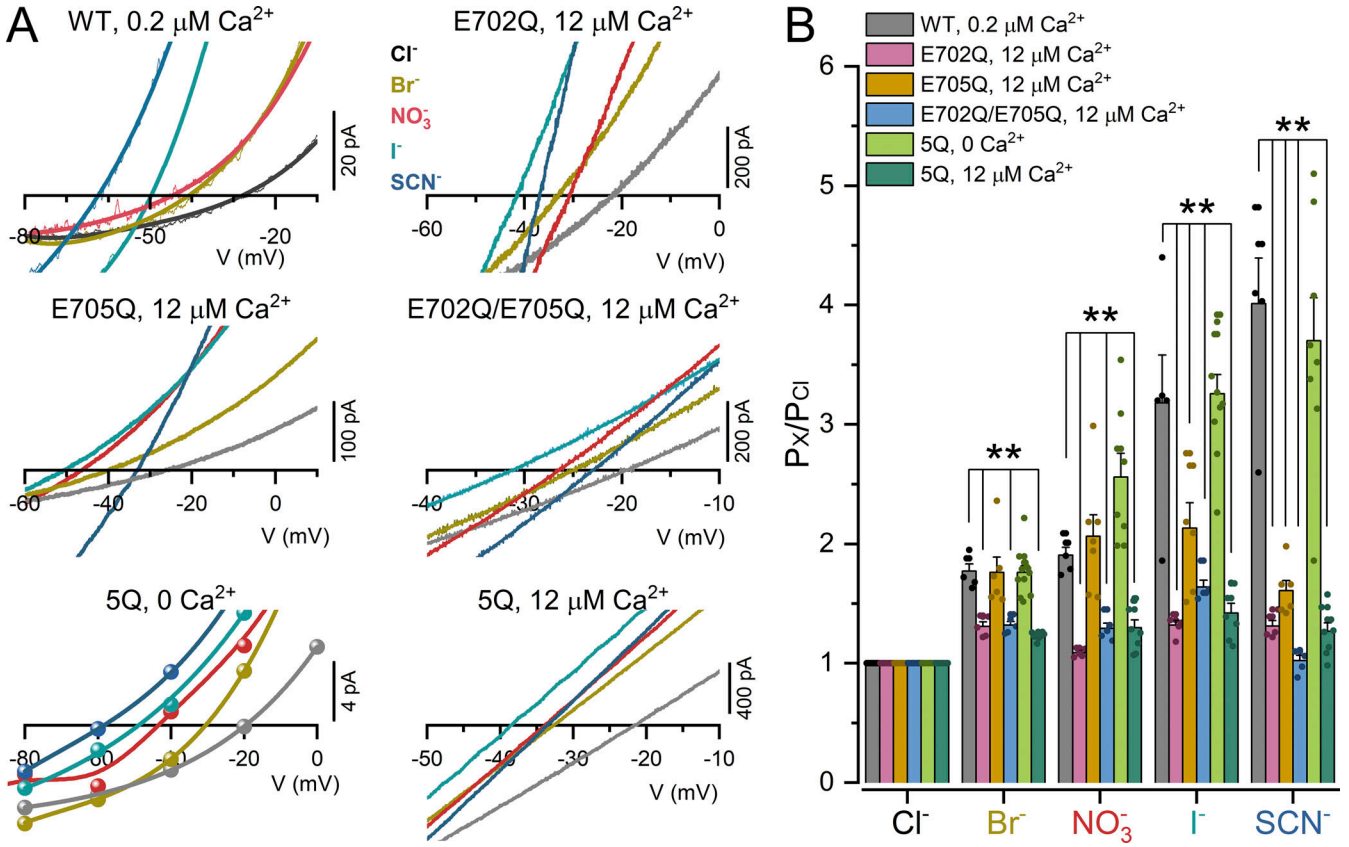

Figure 6. **The Ca^{2+}-pocket of site 1 regulates anion selectivity in TMEM16A. (A)** Six sets of I-V relationships color-coded according to the extracellular solution's anion (top center). Black, Cl^-; olive, Br^-; red, NO_3^-; cyan, I^-; and navy, SCN^-. We used these relationships to determine the reversal potentials of the currents through WT, E702Q, E705Q, E702Q/E705Q, and 5Q mutant channels. Currents were recorded from cells dialyzed with an internal solution containing 0 (5Q), 0.2 (WT), or 12 (E702Q, E705Q, E702Q/E705Q, and 5Q) μM Ca^{2+}. **(B)** Comparison of the anion permeability ratios for WT TMEM16A (gray), E702Q (pink), E705Q (orange), E702Q/E705Q (blue), 5Q without Ca^{2+} (lime green), and 5Q in the presence of Ca^{2+} (sea green). Permeability ratios were calculated from changes of reversal potential induced by the total replacement of extracellular Cl^- with the indicated anions. The permeability ratios were calculated under the following conditions: $[X^-]_e/[Cl^-]_i$ = 140/40 mM and $pH_e = pH_i$ = 7.3. **, P_X/P_{Cl} values were statistically different (P = 0.01) from those corresponding to the WT channel. The data were statistically analyzed using one-way ANOVA with a Tukey's post-hoc test.

anion selectivity sequences for each channel (Table 1). The anion permeability ratios are plotted as gray bars in Fig. 6 B, and the characteristic lyotropic selectivity sequence $SCN^- > I^- > NO_3^- > Br^- > Cl^-$ is listed in the right column of Table 1. The reversal potentials of the currents generated by the E702Q mutant in the presence of Cl^-, Br^-, NO_3^-, I^-, or SCN^- were −22, −33, −31, −41, and −37 mV, respectively. Wider variation in the corresponding values was observed for E705Q (−26, −40, −46, −50, and −33 mV) but not for the double mutant E702Q/E705Q (−20, −25, −26, −31, and −23 mV). The calculated ionic permeability ratios (Table 1) are compared in Fig. 6 B. In general, permeability ratios for NO_3^-, I^-, Br^-, and SCN^- were smaller in the mutants than in the WT TMEM16A recorded in the presence of 0.2 μM Ca^{2+} (Fig. 6 B, gray bars).

Because E702Q and E702/E705Q mutations make the pore nearly unselective to anions, we decided to test the role of the whole acidic residues of site 1 in anion selection by mutating them. For this purpose, we tested the 5Q mutant in the absence and presence of Ca^{2+}. In the absence of intracellular Ca^{2+}, 5Q activity produces small currents at negative potentials (Fig. 6 A, bottom left), displaying an outwardly rectifying open phenotype (Segura-Covarrubias et al., 2020), thus compromising the determination of the reversal potential. To show that 5Q mediated these currents, we recorded I-V relationships in the presence of Cl^- and SCN^- from the same cells exposed to 10 μM DCPIB (4-(2-butyl-6,7-dichlor-2-cyclopentylindan-1-on-5-yl)), an inhibitor of volume-regulated anion channels. Then, we added 0.5 μM ANI9, an inhibitor of TMEM16A, in the presence of DCPIB. ANI9 inhibited the current recorded in the presence of SCN^- without changing the reversal potential, indicating that 5Q activation generates the small currents. Fig. S1 B shows an example of these I-V relations.

Fig. 6 A (bottom left) shows I-V relations obtained in the presence of Cl^-, Br^-, NO_3^-, I^-, or SCN^- from cells dialyzed with solutions without Ca^{2+}. Interestingly, the current reversal potentials and anion selectivity sequence of 5Q in the absence of Ca^{2+} were similar to the WT channel in the presence of 0.2 μM Ca^{2+} (Fig. 6 B, lime green bars; Table 1). This result revealed that the negative charges at the Ca^{2+}-binding site 1 have to be mostly neutralized to allow the channel to discriminate among anions. Then, we determined the anion selectivity in the presence of 12 μM free Ca^{2+} in the cytosolic side. Unexpectedly, the

Table 1. **Ionic permeability ratios (P_X/P_{Cl}) and anion selectivity sequences of WT and mutant TMEM16A channels**

Channel	P_X/P_{Cl}					Selectivity sequence
	SCN^-	NO_3^-	I^-	Br^-	Cl^-	
WT TMEM16A + 0.2 μM Ca^{2+}	4.01 ± 0.38 (5)	1.90 ± 0.06 (5)	3.18 ± 0.40 (5)	1.77 ± 0.06 (5)	1 (5)	$SCN^- > I^- > NO_3^- > Br^- > Cl^-$
I641A – Ca2+	1.67 ± 0.11 (6)	1.22 ± 0.03 (6)	1.92 ± 0.14 (6)	1.43 ± 0.03 (6)	1 (6)	$I^- > SCN^- > Br^- > NO_3^- > Cl^-$
I641A + 0.2 μM Ca^{2+}	1.22 ± 0.05 (6)	1.05 ± 0.05 (6)	1.38 ± 0.05 (6)	1.28 ± 0.03 (6)	1 (6)	$I^- > Br^- = SCN^- > NO_3^- = Cl^-$
G644P + 0.2 μM Ca^{2+}	1.43 ± 0.05 (8)	1.37 ± 0.05 (9)	1.45 ± 0.04 (8)	1.26 ± 0.04 (10)	1 (11)	$SCN^- = I^- = NO_3^- = Br^- > Cl^-$
E702Q + 5 μM Ca^{2+}	1.89 ± 0.18 (7)	1.59 ± 0.11 (7)	1.99 ± 0.11 (6)	1.56 ± 0.06 (6)	1 (32)	$I^- > SCN^- > NO_3^- = Br^- > Cl^-$
E702Q + 12 μM Ca^{2+}	1.31 ± 0.04 (5)	1.09 ± 0.01 (5)	1.32 ± 0.04 (5)	1.31 ± 0.04 (5)	1(5)	$I^- > SCN^- = Br^- > NO_3^- > Cl^-$
E705Q + 12 μM Ca^{2+}	1.60 ± 0.09 (6)	2.06 ± 0.18 (7)	2.13 ± 0.21 (6)	1.76 ± 0.13 (6)	1 (29)	$I^- > NO_3^- > Br^- > SCN^- > Cl^-$
E702Q/E705Q + 12 μM Ca^{2+}	1.02 ± 0.05 (5)	1.29 ± 0.04 (5)	1.64 ± 0.05 (5)	1.32 ± 0.03 (5)	1 (5)	$I^- > NO_3^- > Br^- > SCN^- = Cl^-$
5Q – Ca^{2+}	3.70 ± 0.36 (8)	2.56 ± 0.2 (8)	3.26 ± 0.16 (10)	1.79 ± 0.05 (12)	1 (12)	$SCN^- > I^- > NO_3^- > Br^- > Cl^-$
5Q + 12 μM Ca^{2+}	1.27 ± 0.07 (8)	1.30 ± 0.07 (8)	1.42 ± 0.08 (7)	1.23 ± 0.01 (8)	1 (8)	$SCN^- = I^- = NO_3^- = Br^- \geq Cl^-$
5Q/I641A – Ca^{2+}	1.31 ± 0.05 (7)	0.94 ± 0.03 (5)	1.24 ± 0.03 (6)	1.12 ± 0.01 (6)	1 (7)	$SCN^- > I^- > Br^- > NO_3^- = Cl^-$
5Q/G644P – Ca^{2+}	1.43 ± 0.05 (6)	1.08 ± 0.03 (6)	1.38 ± 0.03 (6)	1.18 ± 0.03 (6)	1 (6)	$SCN^- > I^- > Br^- > NO_3^- > Cl^-$

We computed the permeability ratios using Goldman–Hodgkin–Katz (Eq. 3) and the shifts induced by replacing the total $[Cl^-]_e$ with SCN^-, NO_3^-, I^-, or Br^-. The number of independent reversal potential measurements used to calculate P_X/P_{Cl} is indicated in parentheses. 5Q, channel with five acidic residues of site 1 Ca^{2+} pocket mutated to Q. Pipette solutions contained 0 or the indicated $[Ca^{2+}]_i$ in μM; $[Cl^-]_i$ = 40 mM, pH_e = pH_i = 7.3.

rectification was lost, the current at negative potentials increased, and the zero-current potential values between tested anions were less significant (Fig. 6 A, bottom right). Accordingly, the corresponding P_X/P_{Cl} ratios were <1.5 for all foreign anions (Fig. 6 B, sea green), indicating that 5Q in the presence of 12 μM Ca^{2+} lost anion selectivity. The anion selectivity sequence of this mutant in the presence of Ca^{2+} was $I^- > NO_3^- = SCN^- = Br^- > Cl^-$ (Table 1).

The alterations in anion selectivity produced by single or double Glu (E) to Gln (Q) substitutions were surprising, provided that this procedure presumably only neutralizes the negative charge, similar to titration with Ca^{2+}. As we cancel the charges by a mutation in site 1, the electrostatic potential of the pore should drop until it is completely balanced, as was previously shown using Ca^{2+} in the G644P mutant (Lam and Dutzler, 2018). Therefore, we assumed that the site-directed mutagenesis gradually opened the so-called "electrostatic gate," which is known to hamper anion conduction (Lam and Dutzler, 2018). To find out whether this idea was correct, we calculated the electrostatic potential profiles along the pore for WT, I641A, E702Q, E705Q, E702Q/E705Q, and 5Q channels. To mimic the experimental conditions used to determine the anion selectivity sequences, we performed the calculations in the absence and presence of one or two Ca^{2+} ions in the Ca^{2+} pocket of E702Q, E705Q, and E702Q/E705Q mutant pore structures and without Ca^{2+} in the 5Q. We used the 5OYB structure as a template for replacing the Ca^{2+} pocket residues in silico. In Fig. 7 A, we compare the electrostatic potential profiles obtained.

Overall, electrostatic potentials inverted around the middle of the pore and did not change in the extracellular side. However, compared with WT, we saw significant changes at site 1 and the hydrophobic gate in single and double mutant channels. In the absence of Ca^{2+} (continuous lines), the electrostatic potential became more negative at the site 1 Ca^{2+} pocket region of E702Q, E705Q, and E702Q-E705Q channels. Moreover, in the presence of one Ca^{2+} ion placed near the Ca^{2+} pocket (dotted lines), the potential profiles in these mutants became more positive at the site 1 region but were more negative than the values from the WT profile with two Ca^{2+} ions (black dots). On the other hand, E702/E705 with two Ca^{2+} ions randomly placed near the Ca^{2+} pocket produces a more positive potential profile (dotted blue line; by ~10 kcal/mol). The excess of positive charges due to the presence of the two Ca^{2+} ions could explain this effect. Finally, if the binding of two Ca^{2+} ions balances the electrostatic potential, then 5Q without Ca^{2+} and WT with two Ca^{2+} ions in the pocket should have nearly equal electrostatic potential profiles. Indeed, the electrostatic potential profile of the 5Q pore (continuous red line) was almost the same as that of the WT pore with Ca^{2+} (black dotted line).

This analysis shows that mutating negatively charged residues and increasing Ca^{2+} occupancy in the Ca^{2+} pocket decreases the electrostatic potential in this region. Whether this electrostatic potential drop takes part in the loss of anion selectivity is uncertain. However, it is worth noting that as the electrostatic potential gradually decreases, the channels lose their anion selectivity. Additionally, the electrostatic potentials of WT 0.2 μM Ca^{2+} and 5Q 0 Ca^{2+} are both closer to 0 (neutralized) at site 1 (Fig. 7 B, continuous red line and black dotted line). Functionally, these are the channels that stay selective. This result supports the idea that the electrostatic potential participates in anion selection.

We also compared the electrostatic potential profiles of WT and I641A channels in the absence and presence of Ca^{2+} using the Ca^{2+}-free structure (PDB accession no. 5OYG) of WT TMEM16A (Paulino et al., 2017). The resulting profiles were similar to those previously reported by Lam and Dutzler, (2018). The potential

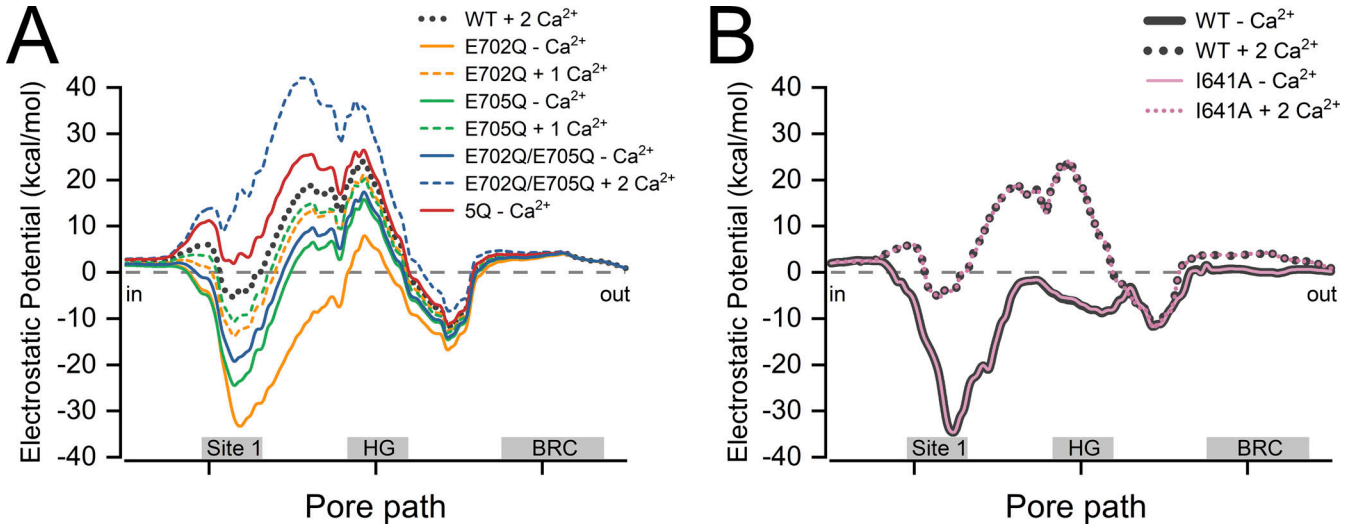

Figure 7. **The electrostatic potential along the pore path of WT, E702Q, E705Q, E702Q/E705Q, 5Q, and I641A channels.** In both plots, the cytosolic and extracellular sides of the pore are on the left and right, respectively. The positions of the high-affinity Ca^{2+} binding site (site 1), hydrophobic gate (HG), and the cluster of basic residues (BRC) are indicated on the horizontal axis (see also Fig. 1). Continuous lines are potential profiles in the absence of Ca^{2+}, and dotted lines are in the presence of the indicated number of Ca^{2+} ions. **(A)** Comparison of the electrostatic potential along the permeation pathway of WT, E702Q, E705Q, E702/E705Q, and 5Q. We made the mutations in silico using the Ca^{2+}-bound structure 5OYB after 30-ns simulation. One Ca^{2+} ion was placed near E705 or E702 in the E702Q or E705Q mutants, respectively. We randomly placed two Ca^{2+} ions near the Ca^{2+} pocket in the double mutant structure. The electrostatic potential of the 5Q pore was calculated using 5OYG as a template to replace the glutamate and aspartate residues. **(B)** Comparison of the electrostatic potential profiles of WT (black) and I641A (pink) channel pores from apo and holo structures. Holo structures keep their two Ca^{2+} ions as found in the cryo-EM structure 5OYB (dotted lines). We used the 5OYG (apo) structure after 30-ns simulation to calculate the electrostatic potential in the absence of Ca^{2+} (continuous lines).

polarity of both pores inverts in the presence of Ca^{2+}, just as in the Ca^{2+}-bound structure 5OYB (Fig. 7 A). In the absence and presence of Ca^{2+} (continuous versus dotted lines, respectively, in Fig. 7 B), the magnitude of the negative and positive potentials was the same in both pores (black versus pink continuous and dotted lines). Note the substantial reduction of the −35 kcal/mol potential around site 1 by adding Ca^{2+}. Also, the potential is inverted around the hydrophobic gate by the presence of Ca^{2+}. However, the total change is minor and, as shown below, the I641A mutation changes anion selectivity, suggesting that the hydrophobic gate sterically contributes to anion selectivity.

In addition to electrostatic, the steric elements in the pore also play a role in controlling the Cl^- conductance (Lam et al., 2021). For example, the structural rearrangements of TM6, after Ca^{2+} binding, control the opening of the hydrophobic gate of TMEM16A channels (Paulino et al., 2017), which participates in anion conduction. Therefore, the TM6 may sterically compromise Cl^- permeation and anion selectivity by partially occluding the apo conformation pore. Consequently, we assessed whether TM6 could be involved in the selectivity process. To this end, we determined the anion selectivity sequence of the single-mutant G644P. This mutation hinders the TM6 hinge flexibility, and the cytosolic half of α-6 presumably adopts an open conformation (Lam and Dutzler, 2018). Additionally, this mutation renders a channel with increased Ca^{2+} sensitivity that can be activated by voltage without intracellular Ca^{2+} (Paulino et al., 2017). Fig. 8 A shows I-V relations around the reversal potentials under different anionic conditions on the extracellular side. Notably, the currents reverted in the narrow voltage range of −35 and −27 mV. This result shows that the G644P mutant channel lost anion selectivity, as corroborated by calculating the permeability ratios for Br^-, NO_3^-, I^-, and SCN^- (Fig. 8 B) and its anion selectivity sequence (Table 1).

The other steric element of TMEM16A gating is the hydrophobic gate, whose opening is coupled to α-6 movement. The I641 is a critical residue for the integrity of the hydrophobic gate (Lam et al., 2021); therefore, we mutated this residue to Ala (A) and determined the anion selectivity to evaluate the role of the gate on the selectivity process. Because the I641A channel has high Ca^{2+} sensitivity and is activated by voltage in the absence of intracellular Ca^{2+}, it allowed us to determine anion selectivity in the absence and presence of 0.2 µM intracellular Ca^{2+} and compare results with those for WT TMEM16A. Fig. 8 C shows I-V relationships around the reversal potential when Cl^-, Br^-, NO_3^-, I^-, or SCN^- was present in the extracellular side. The reversal potentials of the currents generated by cells that expressed the I641A mutant ranged from −29 to −20 mV (upper panel of Fig. 8 C) and from −34 to −20 mV in the absence of intracellular Ca^{2+} (lower panel of Fig. 8 C). Fig. 8 D shows that mutating I641 sharply reduced the permeability ratios and changed the anion selectivity sequence from $SCN^- > I^- > NO_3^- > Br^- > Cl^-$ in WT TMEM16A (gray bars) to $I^- > Br^- \geq SCN^- > NO_3^- > Cl^-$ in the I641A mutant (cyan bars) in the presence of 0.2 µM Ca^{2+} and to $I^- \geq SCN^- > Br^- > NO_3^- > Cl^-$ in I641A in absence of Ca^{2+} (pink bars; Table 1).

To further support the role of the gating elements in anion selectivity, we obtained the permeability ratios in the absence of Ca^{2+} of channels with site 1 and hydrophobic gate (5Q/I641A) or site 1 and TM6 (5Q/G644P) mutated (Fig. 9). As we expected, the shifts in reversal potentials induced by anion replacements in the 5Q/I641A and 5Q/G644P channels (Fig. 9 A) were

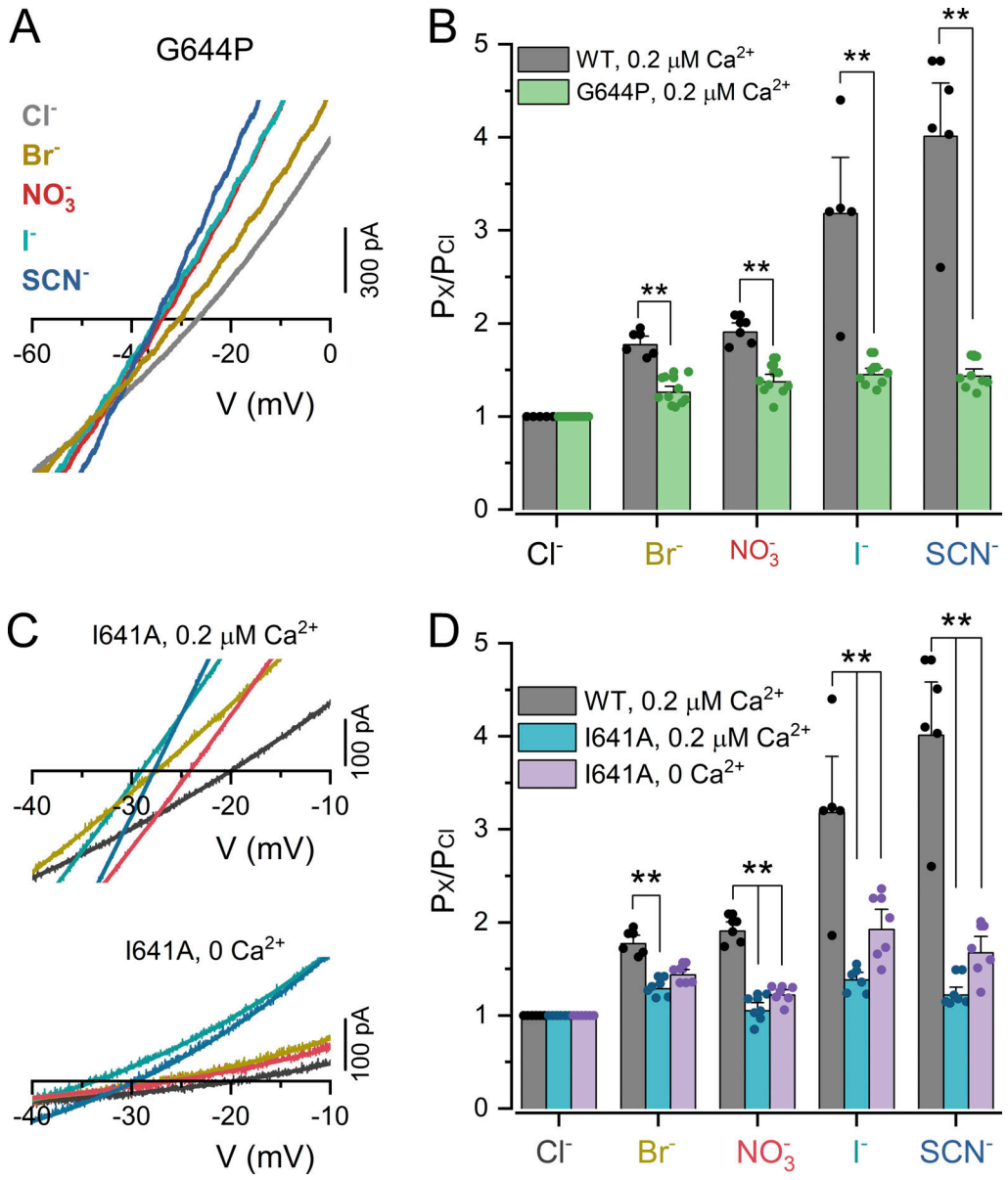

Figure 8. **The TM6 hinge and hydrophobic gate regulate TMEM16A anion selectivity. (A)** Example of I-V relationships used to determine the reversal potentials of the currents through the G644P channel. Currents were recorded from a cell exposed to the indicated anions (top left) and dialyzed with an internal solution containing 0.2 μM Ca^{2+}. **(B)** Comparison of the anion permeability ratios in WT TMEM16A (gray, from Fig. 6) and G644P (green) channels. Permeability ratios were calculated from changes of reversal potentials induced by the total replacement of extracellular Cl^- as shown in A. The permeability ratios were calculated under the following conditions: $[X^-]_e/[Cl^-]_i$ = 140/40 mM and $pH_e = pH_i$ = 7.3. **(C)** Two sets of I-V relationships color-coded according to the extracellular solution's anion. Black, Cl^-; olive, Br^-; red, NO_3^-; cyan, I^-; and navy, SCN^-. The currents were recorded from two cells expressing WT or I641A channels. WT channels were recorded in the presence of 0.2 μM Ca^{2+}, while I641A in 0.2 μM Ca^{2+} and 0 Ca^{2+}. For clarity, only the currents around the reversal potentials are shown, and those were fitted with a polynomial function to determine the reversal potentials by interpolating on the voltage axis. **(D)** Anion permeability ratios for WT and I641A channels calculated from changes of reversal potential induced by the total replacement of extracellular Cl^- with the indicated anions. The permeability ratios were calculated under the following conditions: 0 (I641A) and 0.2 (WT and I641A) μM Ca^{2+}, $[X^-]_e/[Cl^-]_i$ = 140/40 mM and $pH_e = pH_i$ = 7.3. **, P_X/P_{Cl} values for the I641A channel at 0 or 0.2 μM Ca^{2+} were statistically different (P = 0.01) from the WT channels. The data were statistically analyzed using one-way ANOVA with a Tukey's post-hoc test.

significantly reduced compared with 5Q in the absence of Ca^{2+} (Fig. 6 A). However, these reversal potentials were closer to G644P or I641A (Fig. 8). The resulting P_X/P_{Cl} values (Fig. 9 B) and the anion selectivity sequence (Table 1) indicate that both mutants are almost anion unselective.

The 5Q selectivity sequence in the absence of Ca^{2+} is probably like WT, because its gating machinery remained unaltered. Even if site 1 charges are neutralized, if the gating process is changed by mutating either the hydrophobic gate (5Q/I641A) or TM6 movement (G644P-5Q), the channel will become unselective. This comparison highlights the importance of the hydrophobic gate and TM6.

The last column in Table 1 lists anion selectivity sequences for the channels we studied. Mutations at the hydrophobic gate,

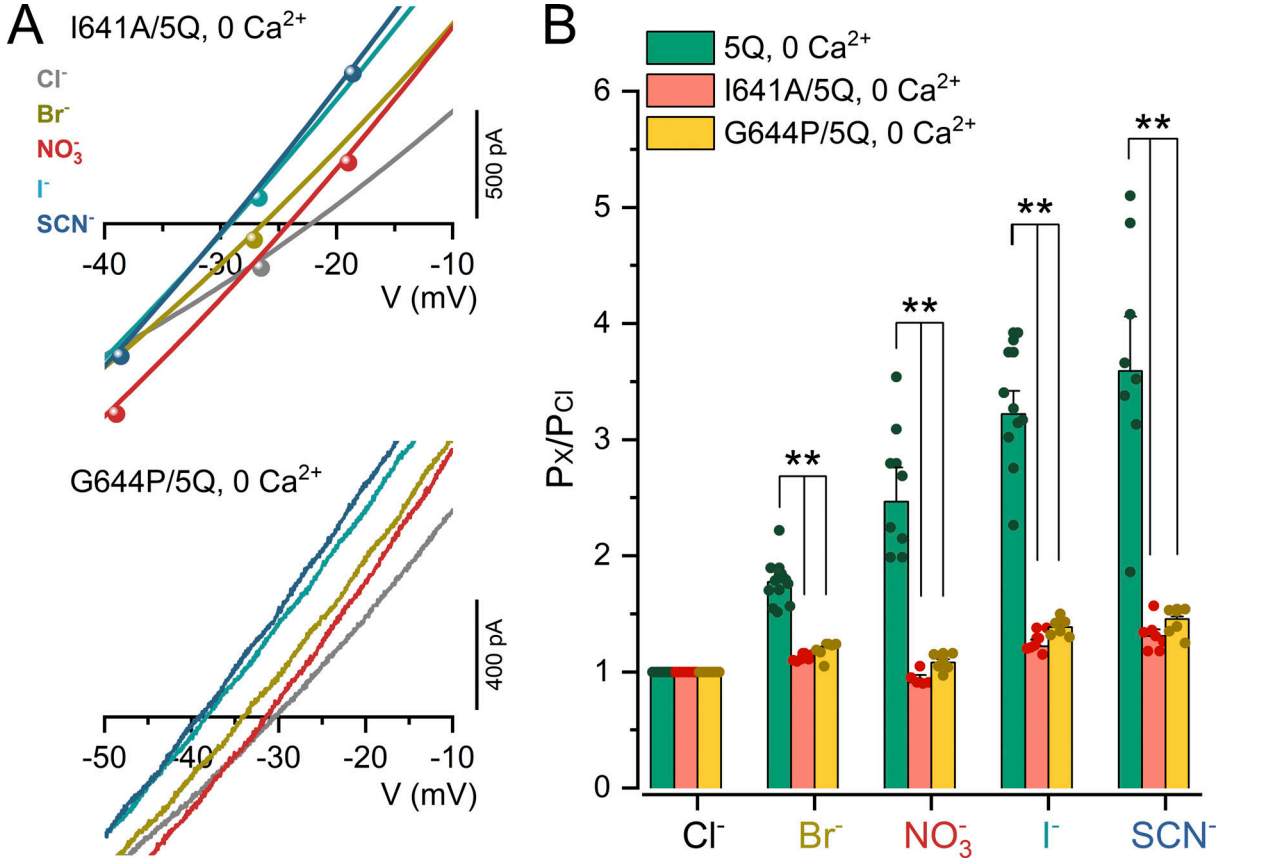

Figure 9. **The gating elements in TMEM16A control the anion selectivity. (A)** I-V relationships for I641A/5Q and G644P/5Q mutant channels. Currents were recorded from cells exposed to the indicated anions (top left) and dialyzed with an internal solution without Ca^{2+}. **(B)** The anion permeability ratios for 5Q (green), I641A/5Q (salmon), and G644P/5Q (yellow) channels. The permeability ratios of the mutant channels were calculated using the changes in reversal potentials obtained from cells dialyzed with a pipette solution without Ca^{2+} as shown in A. The permeability ratios were calculated under the following conditions: $[X^-]_e/[Cl^-]_i$ = 140/40 mM and pH_e = pH_i = 7.3. **, P_X/P_{Cl} values were statistically different (P = 0.01) from those of the 5Q channel at 0 Ca^{2+} (replotted from Fig. 6). The data were statistically analyzed using one-way ANOVA with a Tukey's post-hoc test.

TM6, and site 1 changed the anion selectivity sequence. For example, channels with a mutated hydrophobic gate preferred I^- over other ions and Br^- over NO_3^-, while channels with mutations in site 1 selected I^- and NO_3^- over SCN^-. Taken together, the results of the mutagenesis analysis show that the electrostatic and steric gating elements of TMEM16A control the anion selectivity.

Mutations at the Ca^{2+} pocket and hydrophobic gate modified the facilitation of the voltage dependence caused by SCN^- MFs

Because SCN^- MF facilitated the voltage dependence of WT channels that have their anion selection mechanism intact (Fig. 5), we sought to test whether voltage dependence facilitation is altered in channels made nonselective by mutating their hydrophobic gate (I641A) or site 1 (E702Q-E705Q). We determined the voltage dependence at different external SCN^- MF from cells dialyzed with 0 and 0.2 (I641A) or 12 (E702Q/E705Q) μM Ca^{2+}. Fig. 10, C and E, shows examples of whole-cell currents recorded from two different cells expressing I641A (A) and E702Q/E705Q (C) channels recorded in the presence of Ca^{2+}. The cells were initially in a Cl^--containing solution (black) and then in an SCN^--containing solution (red). Although SCN^- increased both mutants' current, just as in WT channels (see Fig. 5), the effects of SCN^- MF on I641A and E702Q/E705Q differed from WT. For example, the zero-current potentials did not significantly hyperpolarize by increasing SCN^- MF (Fig. 10 G). Consequently, the change in P_{SCN}/P_{Cl} (Fig. 10 H) was negligible in both channels, indicating that channels whose hydrophobic gate or Ca^{2+} pocket was mutated were insensitive to SCN^- MF. Importantly, by increasing the SCN^- MF, the $G/G_{max\_app,\ 0.2\ \mu M\ Ca^{2+}}$-versus-V curves of I641A (Fig. 10 D) shifted toward negative potentials, just like WT channels. However, the $V_{0.5\_app}$ shifts were more significant in the I641A mutant than in WT (when SCN^- MF = 1.00, $V_{0.5\_app}$ was −28 in I641A and +45 mV in WT) with no change in the slope (Fig. 10, I and J, gray spheres). In sharp contrast, the SCN^- MF negligibly altered the $G/G_{max\_app,\ 12\ \mu M\ Ca^{2+}}$-versus-V curves (Fig. 10 F), $V_{0.5\_app}$ (Fig. 10 I), and slope (Fig. 10 J) values in the E702Q/E705Q channel (orange spheres). The complete substitution of Cl^- by SCN^- in this mutant shifted the $G/G_{max\_app,\ 12\ \mu M\ Ca^{2+}}$ curve −30 mV on average and the zero-current potentials by −11 mV. By contrast, the same substitution in the WT channel moved these parameters by −83 and −39 mV, respectively.

A salient result from these experiments is the strong sensitivity of I641A $V_{0.5\_app}$ on SCN^- MF. This result was obtained

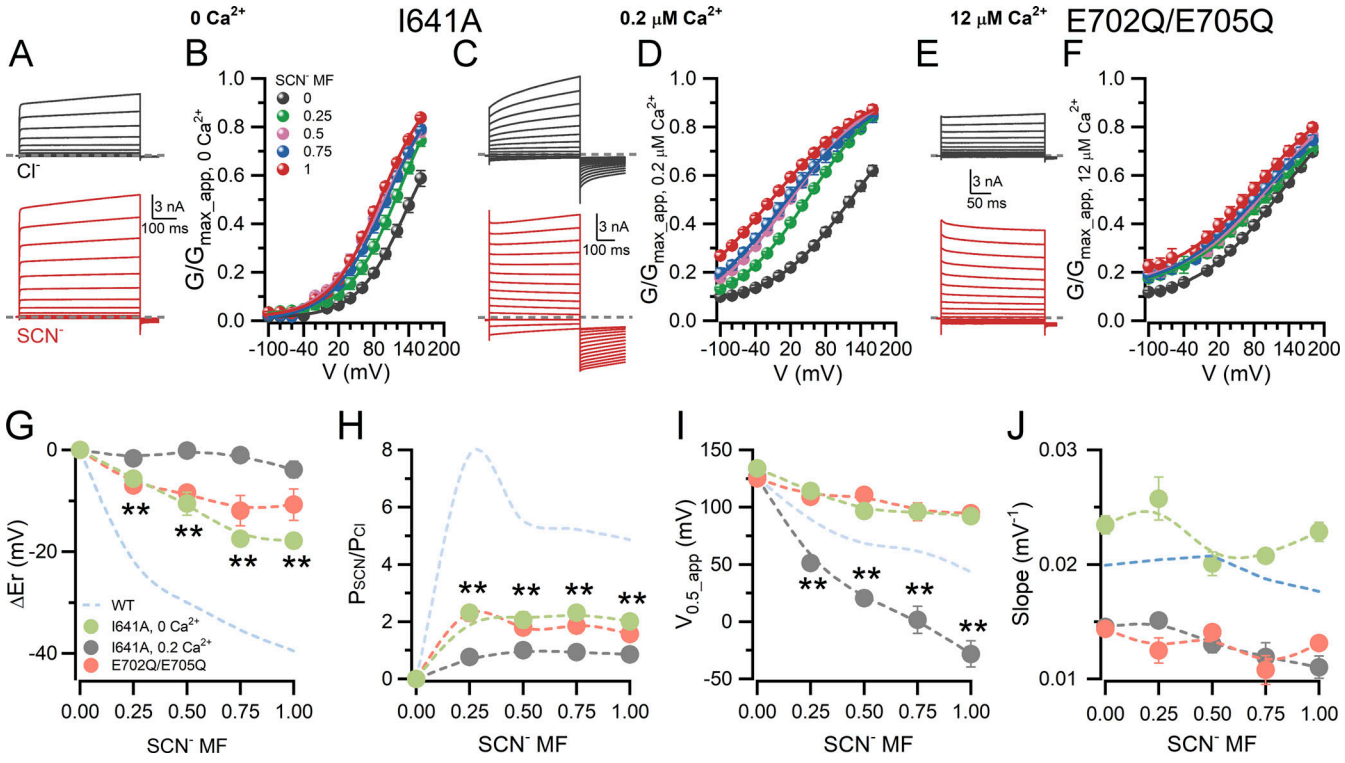

Figure 10. **Mutations at the hydrophobic gate or site 1 alter the facilitation of the voltage dependence induced by extracellular SCN⁻ MFs.** The light blue lines in G–J plots are average WT values replotted from Fig. 5. **(A, C, and E)** Macroscopic currents recorded from cells expressing I641A and E702Q/E705Q channels. Each pair was obtained from the same cell dialyzed with 0 or 0.2 (I641A) or 12 (E702Q/E705Q) µM Ca^{2+} in the presence of extracellular Cl^- (black) and then in the presence of SCN^- (red). Scale bars are valid for both sets of traces. Gray lines indicate the zero-current levels. **(B, D, and F)** Voltage dependence of normalized conductance of I641A (B and D) and E702Q/E705Q (D) channels calculated from recordings obtained in the presence of the indicated SCN^- MF in B. For I641A in 0 Ca^{2+}, I641A in 0.2 µM Ca^{2+}, and E702Q/E705Q in 12 µM Ca^{2+} were n = 19, 23, and 24 (SCN^- MF = 0); 5, 9, and 7 (SCN^- MF = 0.25); 5, 8, and 10 (SCN^- MF = 0.5); 5, 5, and 6 (SCN^- MF = 0.75); and 4, 6, and 6 (SCN^- MF = 1.0), respectively. The continuous lines are fits with the logistic Eq. 2 to determine $V_{0.5\_app}$ and slope values. **(G)** Changes of reversal potential induced by SCN^- MF on currents generated by I641A in 0 Ca^{2+} (lime green), I641A in 0.2 µM Ca^{2+} (gray), and E702Q/E705Q in 12 µM Ca^{2+} (salmon) channels. **, ΔEr values for the I641A and E702Q/E705Q channels were statistically different (P = 0.01) from those corresponding to WT (blue line). Data were analyzed using one-way ANOVA with a Tukey's post-hoc test. **(H)** P_{SCN}/P_{Cl} for I641A in 0 Ca^{2+} (lime green), I641A in 0.2 µM Ca^{2+} (gray), and E702Q/E705Q in 12 µM Ca^{2+} (salmon) channels at different SCN^- MF. Permeability ratios were calculated using the Goldman–Hodgkin–Katz equation and the changes of reversal potential shown in G. **(I)** $V_{0.5\_app}$ at different SCN^- MF determined for I641A in 0 Ca^{2+} (lime green), I641A in 0.2 µM Ca^{2+} (gray), and E702Q/E705Q in 12 µM Ca^{2+} (salmon) channels. Values were obtained from fits shown in B, D, and F. **, $V_{0.5\_app}$ values for the I641A channel in the presence of Ca^{2+} were statistically different (P = 0.01) from those obtained with 0 SCN^- MF. Data were analyzed using one-way ANOVA with a Tukey's post-hoc test. **(J)** Slope values at different SCN^- MF determined for I641A in 0 Ca^{2+} (lime green), I641A in 0.2 µM Ca^{2+} (gray), and E702Q/E705Q in 12 µM Ca^{2+} (salmon) channels. Values were obtained from fits shown in B, D, and F.

from experiments performed in the presence of intracellular Ca^{2+}; thus, we presume that Ca^{2+} still binds to site 1 because it is unaltered in the I641A mutant. Moreover, this mutant displays higher sensitivity for Ca^{2+} than WT (Peters et al., 2018). Thus, we suppose that permeant SCN^- would stabilize the Ca^{2+} bound to site 1, as previously shown in WT channels (Fig. 4), hence increasing the voltage sensitivity. To evaluate this idea, we repeated an SCN^- MF experiment recording the I641A mutant without intracellular Ca^{2+}. Fig. 10 A shows that the current is enhanced by replacing the extracellular Cl^- with SCN^-. However, the $G/G_{max\_app,\ 0\ \mu M\ Ca^{2+}}$-versus-V curves (Fig. 10 B) and their $V_{0.5\_app}$ (Fig. 10 I, lime symbols) were not strongly affected by the SCN^- MF. Also, the change in reversal potential was less than −20 mV after the total substitution of Cl^- with SCN^- (Fig. 10 G). P_{SCN}/P_{Cl} ratios were ∼2 with different SCN^- MF (Fig. 10 H). Interestingly, the slope remained at ∼0.03 mV^{-1} (Fig. 10 J), a value slightly higher than the one for WT channels (0.02 mV^{-1}).

In conclusion, these data demonstrate that mutations at the hydrophobic gate or site 1 not only hinder anion selectivity but also alter the ability of the channel to change its voltage dependence when highly permeant anions are present.

Discussion

This work describes that permeable anions increase the Ca^{2+} sensitivity of TMEM16A as their permeability ratio increases, presumably by stabilizing Ca^{2+} binding to site 1 (an essential step to start the gating process). Conversely, mutations at the Ca^{2+} binding site 1, TM6 hinge, and hydrophobic gate turned TMEM16A unselective, thus revealing the essential role of the gating elements as structural determinants of anion selectivity.

Overall, our data point to a reciprocal interaction between permeant anions and gating.

A critical aspect for understanding the permeant anions' role in TMEM16A gating, and probably in TMEM16B too, is that site 1 is next to the permeation pathway, thus enabling a two-way interaction (Lam and Dutzler, 2018). On the one hand, permeant anions in the pore or near the Ca^{2+} pocket stabilize Ca^{2+} ligation, thus enhancing the apparent Ca^{2+} sensitivity. On the other hand, the gating elements of TMEM16A control anion selectivity. This mutually affecting interaction within the pore is in agreement with present and previous results showing that (1) anions more permeable than Cl^- as well as SCN^- MF increase the apparent Ca^{2+} sensitivity and slow the off-rate of Ca^{2+}-induced currents; (2) the apparent Ca^{2+} sensitivity shows AMF behavior; (3) mutations at the gating elements make TMEM16A nonselective and alter the SCN^--dependent regulation of voltage dependence; (4) Cl^- conductance is facilitated by neutralizing site 1 electrostatic potential with Ca^{2+} (Lam and Dutzler, 2018); (5) P_I/P_{Cl} and P_{SCN}/P_{Cl} decrease in the WT channel upon increase of the intracellular Ca^{2+} concentration (Peters et al., 2015); (6) the apparent Ca^{2+} affinity of TMEM16A increases by neutralizing or reversing the charge of K588 and K645 adjacent to site 1 (Lam and Dutzler, 2018); (7) the on and off of the Ca^{2+}-activated Cl^- currents from parotid acinar cells are accelerated and slowed, respectively, by permeant anions (Perez-Cornejo et al., 2004); (8) intracellular SCN^- increases the apparent Ca^{2+} sensitivity of Ca^{2+}-activated Cl^- currents in *Xenopus* oocytes (Qu and Hartzell, 2000); (9) anions with higher permeability than Cl^- increase the apparent Ca^{2+} sensitivity of TMEM16B (Betto et al., 2014); and (10) dynamic anion selectivity is observed in TMEM16B exposed to Ca^{2+} jumps (Sagheddu et al., 2010). These results strongly suggest that permeation and Ca^{2+} ligation are coupled and highlight the critical role of permeant anions in TMEM16A activation. Alternatively, anions could hamper the conformational transition of α-6 following Ca^{2+} binding or the closing of the hydrophobic gate instead of directly interacting with the Ca^{2+}-sensing machinery, thus slowing channel closure.

Other channels have a gating mechanism that shows dependence on the permeant ion. For example, in voltage-gated Cl^- channels CLC-0 and CLC-1, a Cl^- ion could be responsible for opening a glutamate gate protruding the permeation pathway (Pusch et al., 1995; Chen and Miller, 1996; Chen, 2003; Pusch, 1996; Rychkov et al., 2001). Furthermore, we showed that the interaction between the hyperpolarization-propelled intracellular Cl^- and the pore gate triggers CLC-2 gating (De Jesús-Pérez et al., 2016, 2021; Sánchez-Rodríguez et al., 2010, 2012). In TMEM16B, highly permeable anions facilitated the voltage-gated opening and increased the apparent Ca^{2+} sensitivity (Betto et al., 2014). Furthermore, we reported that the slow gating mode of TMEM16A and the process by which TMEM16A reaches full conduction depend on Cl^- ions (Contreras-Vite et al., 2016; Cruz-Rangel et al., 2017). Thus, the previous data and the present work indicate that in TMEM16A and TMEM16B Cl^- channels, the permeant anion plays an essential role in gating.

It was previously established that the extracellular entrance and the narrow neck of the pore (Fig. 1) take part in anion selection in TMEM16A. Alanine scanning of the extracellular residues R511, K599, R617, and R784 located in α-3, α-5, α-5–α-6 linker, and α-9, respectively, showed that the P_I/P_{Cl} and P_{SCN}/P_{Cl} increased without altering the apparent Ca^{2+} sensitivity, but, in the same mutants, P_{SCN}/P_{Cl} increased by raising the $[Ca^{2+}]_i$ from 400 nM to 1 mM (Peters et al., 2015). Furthermore, mutation of two lysines, K584 and K645 in TMEM16A (a; K588 and K649 in TMEM16A [ac], respectively) located at the narrow neck modulated channel rectification and ion permeation under extremely high Ca^{2+} concentrations to neutralize the electrostatic potential generated by the Ca^{2+} pocket (Reyes et al., 2015; Lam and Dutzler, 2018). In addition, varying the electrostatic potential of the pore changes the anion conductance of TMEM16A (Nguyen et al., 2019; Lim et al., 2016; Jeng et al., 2016). Here, we report that anion selectivity is controlled by the gating elements of TMEM16A: the Ca^{2+} binding pocket of site 1, TM6, and the hydrophobic gate. Thus, the anion selectivity process by TMEM16A occurs at five structural domains along the pore: one located on the extracellular side formed by four basic residues, and four inside the pore, including (1) the hydrophobic gate, (2) two lysines at the narrow neck, (3) site 1, and (4) the cytosolic side of the TM6 (Fig. 1). Thus, anion selection in TMEM16A occurs along the narrow section of the pore, a process similar to that described in BEST1, another Ca^{2+}-activated Cl^- channel (Vaisey et al., 2016).

The anion selectivity mechanism of TMEM16A is poorly understood. The consensus anion selectivity sequence determined from the reversal potentials of macroscopic currents recorded from different native cells expressing endogenous CaCC or cells expressing cloned TMEM16A is $SCN^- > I^- > NO_3^- > Br^- > Cl^-$ (Evans and Marty, 1986; Large and Wang, 1996; Yang et al., 2008; Schroeder et al., 2008; Adomaviciene et al., 2013; Ni et al., 2014; Qu and Hartzell, 2000; Perez-Cornejo et al., 2004; Berg et al., 2012). This lyotropic sequence has been reported in different anion channels (Large and Wang, 1996) and suggests a selectivity mechanism for a pore that contains weak field strength binding sites (Wright and Diamond, 1977). Our data indicate that neutralizing the negative charges at site 1 is necessary for TMEM16A channels to present their characteristic lyotropic selective sequence. However, it seems unlikely that these charges are part of the binding sites. Unlike K^+ channels (Gouaux and Mackinnon, 2005), TMEM16A structures do not reveal Cl^- ions within the permeation pathway (Paulino et al., 2017), thus making it challenging to find the pore domains involved in ion binding and their physical-chemistry properties. Molecular dynamics simulations show that Cl^- paused at the two regions of the pore during the permeation (Jia and Chen, 2021). However, no coordination between Cl^- and pore residues was determined. Instead, the simulation suggests that the hydrophobic portion of the neck generates energy barriers for Cl^- permeation that are lower for SCN^- due to its lower hydration energy. More structural data are needed to determine the Cl^- binding sites within the TMEM16A pore and its relation to Cl^- permeation.

The poor anion selectivity and the linear relationship between permeability ratios and anion hydration energies suggest that the anion dehydration energy determines a weak interaction between the permeant anion and putative binding sites within the WT TMEM16A pore (Dawson et al., 1999; Perez-Cornejo et al., 2004; Qu and Hartzell, 2000). Interestingly,

molecular dynamics simulations showed that a single Cl^- ion permeates the entire TMEM16A pore surrounded by four to five water molecules at the narrow neck and six to seven water molecules at the vestibules (Jia and Chen, 2021). This observation would suggest that Cl^- permeates the pore in the hydrated state. Furthermore, we found that channels with their hydrophobic gate, TM6, and Ca^{2+} pocket mutated lost the linear relationship between permeability ratios and anion hydration energy (Fig. S2). This observation indicates that the tested anions experience almost equal energy barriers during the permeation process through mutant pores. Our finding that channels with a mutated Ca^{2+} pocket display similar electrostatic potential profiles supports this conclusion.

Interestingly, SCN^- and I^-, the most permeable anions through TMEM16A, can be oxidized to produce antimicrobial compounds in secretory glands and the extracellular fluid layer of the airways. This oxidation process is caused by the hydrogen peroxide produced by dual oxidase 1/thyroid oxidase 1 and dual oxidase 2/thyroid oxidase 2 (Geiszt et al., 2003). In normal conditions, it is estimated that the airway secretions could have ≤0.4 mM SCN^- (Fragoso et al., 2004), which dual oxidases can use as a source for manufacturing bactericides. This high concentration of extracellular SCN^- is partly maintained by the elevated SCN^- permeability of the CFTR Cl^- channel (Moskwa et al., 2007). However, in cystic fibrosis patients, this antibacterial system is inoperative (Moskwa et al., 2007). Therefore, TMEM16A, which is expressed along with CFTR in airway epithelial cells, could serve as a CFTR surrogate to maintain the extracellular SCN^- concentration and sustain the microbicidal function (Pedemonte et al., 2007). However, the role of TMEM16A in this defense mechanism is unclear. The permeability of TMEM16A to SCN^- and I^- and the production of antimicrobial substances would be compromised if residues controlling the hydrophobic and site 1 are mutated or by pharmacological interventions targeting the hydrophobic gate (Dinsdale et al., 2021). However, mutations of the four extracellular basic residues can upregulate the permeability to SCN^- and I^- (Peters et al., 2015). Therefore, additional experiments aimed at testing the role of TMEM16A in this defense system are required.

In conclusion, we present evidence that anion selectivity occurs along the pore of TMEM16A. Also, we show that reciprocal interaction between permeant anions and the gating elements alter the Ca^{2+} sensitivity, voltage dependence, and the anion selectivity of TMEM16A. This type of regulation likely impacts the mean open time of the channels, ultimately tuning anion flux during physiological responses. In addition, these data add to the growing body of evidence supporting the idea that permeant anions play an active role in ion channel gating.

Data availability

The data that support the findings of this study are available from the corresponding author upon reasonable request.

Acknowledgments

Joseph A. Mindell served as editor.

The authors thank C.Y. Hernandez-Carballo for technical assistance.

The work was supported by grant FORDECYT-PRONACES (Ciencia de Frontera 2019) 1308052 2020 from CONACyT, México. J.J. De Jesús-Pérez was supported by a Graduate Student Fellowship #234820 and Postdoctoral Fellowship #711128 from CONACyT, México. O. Posadas was supported by a Graduate Student Fellowship # 933084 from CONACyT, México. G. Segura-Covarrubias was supported by a Graduate Student Fellowship # 297721 from CONACyT, México.

The authors declare no competing financial interests.

Author contributions: All experiments described in this manuscript were performed at the Institute of Physics of the Universidad Autonoma de San Luis Potosi. J.J. De Jesús-Pérez: Design of the work, acquisition, analysis, and interpretation of data, and revising the manuscript critically for important intellectual content. A.E. López-Romero: Acquisition, analysis, and interpretation of data, and revising the manuscript critically. O. Posadas: Acquisition, analysis, and interpretation of data, and revising the manuscript critically. G. Segura-Covarrubias: Acquisition, analysis, and interpretation of data, and revising the manuscript critically. I. Aréchiga-Figueroa: Acquisition, analysis, and interpretation of data, revising the manuscript critically for important intellectual content, and securing funds to support the project. B. Gutiérrez-Medina: Interpretation of data and revising the manuscript critically for important intellectual content. P. Pérez-Cornejo: Design of the work, interpretation of data, revising the manuscript critically for important intellectual content, and securing funds to support the project. J. Arreola: Conception and design of the work, analysis and interpretation of data, drafting the work and revising it critically for important intellectual content, and securing funds to support the project.

Submitted: 17 September 2021
Accepted: 23 May 2022

References

Adomaviciene, A., K.J. Smith, H. Garnett, and P. Tammaro. 2013. Putative pore-loops of TMEM16/anoctamin channels affect channel density in cell membranes. *J. Physiol.* 591:3487–3505. https://doi.org/10.1113/jphysiol.2013.251660

Arreola, J., J.E. Melvin, and T. Begenisich. 1996. Activation of calcium-dependent chloride channels in rat parotid acinar cells. *J. Gen. Physiol.* 108:35–47. https://doi.org/10.1085/jgp.108.1.35

Berg, J., H.H. Yang, and L.Y. Jan. 2012. Ca^{2+}-activated Cl^- channels at a glance. *J. Cell Sci.* 125:1367–1371. https://doi.org/10.1242/jcs.093260

Betto, G., O.L. Cherian, S. Pifferi, V. Cenedese, A. Boccaccio, and A. Menini. 2014. Interactions between permeation and gating in the TMEM16B/anoctamin2 calcium-activated chloride channel. *J. Gen. Physiol.* 143:703–718 https://doi.org/10.1085/jgp.201411182

Chen, T.-Y. 2003. Coupling gating with ion permeation in ClC channels. *Sci. STKE.* 2003:pe23 https://doi.org/10.1126/stke.2003.188.pe23

Chen, T.Y., and C. Miller. 1996. Nonequilibrium gating and voltage dependence of the ClC-0 Cl^- channel. *J. Gen. Physiol.* 108:237–250. https://doi.org/10.1085/jgp.108.4.237

Contreras-Vite, J.A., S. Cruz-Rangel, J.J. De Jesús-Pérez, I.A.A. Figueroa, A.A. Rodríguez-Menchaca, P. Pérez-Cornejo, H.C. Hartzell, and J. Arreola. 2016. Revealing the activation pathway for TMEM16A chloride channels from macroscopic currents and kinetic models. *Pflugers Arch.* 468:1241–1257. https://doi.org/10.1007/s00424-016-1830-9

Cruz-Rangel, S., J.J. De Jesús-Pérez, I.A. Aréchiga-Figueroa, A.A. Rodríguez-Menchaca, P. Pérez-Cornejo, H.C. Hartzell, and J. Arreola. 2017. Extracellular protons enable activation of the calcium-dependent chloride channel TMEM16A. *J. Physiol.* 595:1515–1531. https://doi.org/10.1113/JP273111

Dang, S., S. Feng, J. Tien, C.J. Peters, D. Bulkley, M. Lolicato, J. Zhao, K. Zuberbühler, W. Ye, L. Qi, et al. 2017. Cryo-EM structures of the TMEM16A calciumactivated chloride channel. *Nature*. 552:426–429. https://doi.org/10.1038/nature25024

Dawson, D.C., S.S. Smith, and M.K. Mansoura. 1999. CFTR: Mechanism of anion conduction. *Physiol. Rev.* 79:S47–S75. https://doi.org/10.1152/physrev.1999.79.1.S47

Dinsdale, R.L., T. Pipatpolkai, E. Agostinelli, A.J. Russell, P.J. Stansfeld, and P. Tammaro. 2021. An outer-pore gate modulates the pharmacology of the TMEM16A channel. *Proc. Natl. Acad. Sci. USA*. 118:e2023572118. https://doi.org/10.1073/pnas.2023572118

Duran, C., C.H. Thompson, Q. Xiao, and H.C. Hartzell. 2010. Chloride channels: Often enigmatic, rarely predictable. *Annu. Rev. Physiol.* 72:95–121. https://doi.org/10.1146/annurev-physiol-021909-135811

Evans, M.G., and A. Marty. 1986. Calcium-dependent chloride currents in isolated cells from rat lacrimal gland. *J. Physiol.* 378:437–460. https://doi.org/10.1113/jphysiol.1986.sp016229

Fragoso, M.A., V. Fernandez, R. Forteza, S.H. Randell, M. Salathe, and G.E. Conner. 2004. Transcellular thiocyanate transport by human airway epithelia. *J. Physiol.* 561:183–194. https://doi.org/10.1113/jphysiol.2004.071548

Geiszt, M., J. Witta, J. Baffi, K. Lekstrom, and T.L. Leto. 2003. Dual oxidases represent novel hydrogen peroxide sources supporting mucosal surface host defense. *FASEB J.* 17:1502–1504. https://doi.org/10.1096/fj.02-1104fje

Gouaux, E., and R. Mackinnon. 2005. Principles of selective ion transport in channels and pumps. *Science*. 310:1461–1465. https://doi.org/10.1126/science.1113666

Hartzell, C., I. Putzier, and J. Arreola. 2005. Calcium-activated chloride channels. *Annu. Rev. Physiol.* 67:719–758. https://doi.org/10.1146/annurev.physiol.67.032003.154341

Hernández-Carballo, C.Y., J.A. De Santiago-Castillo, T. Rosales-Saavedra, P. Pérez-Cornejo, and J. Arreola. 2010. Control of volume-sensitive chloride channel inactivation by the coupled action of intracellular chloride and extracellular protons. *Pflugers Arch.* 460:633–644. https://doi.org/10.1007/s00424-010-0842-0

Im, W., D. Beglov, and B. Roux. 1998. Continuum solvation model: Computation of electrostatic forces from numerical solutions to the Poisson-Boltzmann equation. *Comput. Phys. Commun.* 111:59–75. https://doi.org/10.1016/s0010-4655(98)00016-2

Jeng, G., M. Aggarwal, W.P. Yu, and T.Y. Chen. 2016. Independent activation of distinct pores in dimeric TMEM16A channels. *J. Gen. Physiol.* 148:393–404. https://doi.org/10.1085/jgp.201611651

De Jesús-Pérez, J.J., A. Castro-Chong, R.C. Shieh, C.Y. Hernández-Carballo, J.A. De Santiago-Castillo, and J. Arreola. 2016. Gating the glutamate gate of CLC-2 chloride channel by pore occupancy. *J. Gen. Physiol.* 147:25–37. https://doi.org/10.1085/jgp.201511424

De Jesús-Pérez, J.J., G.A. Méndez-Maldonado, A.E. López-Romero, D. Esparza-Jasso, I.L. González-Hernández, V. De la Rosa, R. Gastélum-Garibaldi, J.E. Sánchez-Rodríguez, and J. Arreola. 2021. Electro-steric opening of the clc-2 chloride channel gate. *Sci. Rep.* 11:13127. https://doi.org/10.1038/s41598-021-92247-3

Jia, Z., and J. Chen. 2021. Specific PIP2 binding promotes calcium activation of TMEM16A chloride channels. *Commun. Biol.* 4:259. https://doi.org/10.1038/s42003-021-01782-2

Jo, S., T. Kim, V.G. Iyer, and W. Im. 2008a. CHARMM-GUI: A web-based graphical user interface for CHARMM. *J. Comput. Chem.* 29:1859–1865. https://doi.org/10.1002/jcc.20945

Jo, S., M. Vargyas, J. Vasko-Szedlar, B. Roux, and W. Im. 2008b. PBEQ-Solver for online visualization of electrostatic potential of biomolecules. *Nucleic Acids Res.* 36:270–275. https://doi.org/10.1093/nar/gkn314

Lam, A.K.M., and R. Dutzler. 2018. Calcium-dependent electrostatic control of anion access to the pore of the calcium-activated chloride channel TMEM16A. *Elife*. 7:e39122. https://doi.org/10.7554/elife.39122

Lam, A.K.M., J. Rheinberger, C. Paulino, and R. Dutzler. 2021. Gating the pore of the calcium-activated chloride channel TMEM16A. *Nat. Commun.* 12:785. https://doi.org/10.1038/s41467-020-20787-9

Large, W.A., and Q. Wang. 1996. Characteristics and physiological role of the $Ca^{(2+)}$-activated Cl^- conductance in smooth muscle. *Am. J. Physiol.* 271:C435–C454. https://doi.org/10.1152/ajpcell.1996.271.2.C435

Le, S.C., and H. Yang. 2020. An additional Ca^{2+} binding site allosterically controls TMEM16A activation. *Cell Rep.* 33:108570. https://doi.org/10.1016/j.celrep.2020.108570

Lim, N.K., A.K.M. Lam, and R. Dutzler. 2016. Independent activation of ion conduction pores in the double-barreled calcium-activated chloride channel TMEM16A. *J. Gen. Physiol.* 148:375–392. https://doi.org/10.1085/jgp.201611650

Marcus, Y. 1997. Ion Properties. Marcel Dekker, New York.

Moskwa, P., D. Lorentzen, K.J.D.A. Excoffon, J. Zabner, P.B. McCray, W.M. Nauseef, C. Dupuy, and B. Bánfi. 2007. A novel host defense system of airways is defective in cystic fibrosis. *Am. J. Respir. Crit. Care Med.* 175:174–183. https://doi.org/10.1164/rccm.200607-1029oc

Murray, J.S., and P. Politzer. 2017. Molecular electrostatic potentials and noncovalent interactions. *Wiley Interdiscip. Rev.* 7:e1326. https://doi.org/10.1002/wcms.1326

Neher, E. 1992. Correction for liquid junction potentials in patch clamp experiments. *Methods Enzymol.* 207:123–131. https://doi.org/10.1016/0076-6879(92)07008-c

Nguyen, D.M., L.S. Chen, W.P. Yu, and T.Y. Chen. 2019. Comparison of ion transport determinants between a TMEM16 chloride channel and phospholipid scramblase. *J. Gen. Physiol.* 151:518–531. https://doi.org/10.1085/jgp.201812270

Ni, Y.L., A.S. Kuan, and T.Y. Chen. 2014. Activation and inhibition of TMEM16A calcium-activated chloride channels. *PLoS One*. 9:e86734. https://doi.org/10.1371/journal.pone.0086734

Paulino, C., V. Kalienkova, A.K.M. Lam, Y. Neldner, and R. Dutzler. 2017. Activation mechanism of the calcium-activated chloride channel TMEM16A revealed by cryo-EM. *Nature*. 552:421–425. https://doi.org/10.1038/nature24652

Pedemonte, N., and L.J.V. Galietta. 2014. Structure and function of TMEM16 proteins (anoctamins). *Physiol. Rev.* 94:419–459. https://doi.org/10.1152/physrev.00039.2011

Pedemonte, N., E. Caci, E. Sondo, A. Caputo, K. Rhoden, U. Pfeffer, M. Di Candia, R. Bandettini, R. Ravazzolo, O. Zegarra-Moran, and L.J.V. Galietta. 2007. Thiocyanate transport in resting and IL-4-stimulated human bronchial epithelial cells: Role of pendrin and anion channels. *J. Immunol.* 178:5144–5153. https://doi.org/10.4049/jimmunol.178.8.5144

Perez-Cornejo, P., J.A. De Santiago, and J. Arreola. 2004. Permeant anions control gating of calcium-dependent chloride channels. *J. Membr. Biol.* 198:125–133. https://doi.org/10.1007/s00232-004-0659-x

Peters, C.J., J.M. Gilchrist, J. Tien, N.P. Bethel, L. Qi, T. Chen, L. Wang, Y.N. Jan, M. Grabe, and L.Y. Jan. 2018. The sixth transmembrane segment is a major gating component of the TMEM16A calcium-activated chloride channel. *Neuron*. 97:1063–1077.e4. https://doi.org/10.1016/j.neuron.2018.01.048

Peters, C.J., H. Yu, J. Tien, Y.N. Jan, M. Li, and L.Y. Jan. 2015. Four basic residues critical for the ion selectivity and pore blocker sensitivity of TMEM16A calcium-activated chloride channels. *Proc. Natl. Acad. Sci. USA*. 112:3547–3552. https://doi.org/10.1073/pnas.1502291112

Pusch, M. 1996. Knocking on channel's door the permeating chloride ion acts as the gating charge in ClC-0. *J. Gen. Physiol.* 108:233–236. https://doi.org/10.1085/jgp.108.4.233

Pusch, M., U. Ludewig, A. Rehfeldt, and T.J. Jentsch. 1995. Gating of the voltage-dependent chloride channel CIC-0 by the permeant anion. *Nature*. 373:527–531. https://doi.org/10.1038/373527a0

Qu, Z., and H.C. Hartzell. 2000. Anion permeation in Ca^{2+}-activated Cl^- channels. *J. Gen. Physiol.* 116:825–844. https://doi.org/10.1085/jgp.116.6.825

Reyes, J.P., A.Huanosta-Gutiérrez, A. López-Rodríguez, and A. Martínez-Torres. 2015. Study of permeation and blocker binding in TMEM16A calcium-activated chloride channels. *Channels*. 9:88–95. https://doi.org/10.1080/19336950.2015.1027849

Rychkov, G.Y., M. Pusch, M.L. Roberts, and A.H. Bretag. 2001. Interaction of hydrophobic anions with the rat skeletal muscle chloride channel ClC-1: Effects on permeation and gating. *J. Physiol.* 530:379–393. https://doi.org/10.1111/j.1469-7793.2001.0379k.x

Sagheddu, C., A. Boccaccio, M. Dibattista, G. Montani, R. Tirindelli, and A. Menini. 2010. Calcium concentration jumps reveal dynamic ion selectivity of calcium-activated chloride currents in mouse olfactory sensory neurons and TMEM16b-transfected HEK 293T cells. *J. Physiol.* 588:4189–4204. https://doi.org/10.1113/jphysiol.2010.194407

Sánchez-Rodríguez, J.E., J.A. De Santiago-Castillo, and J. Arreola. 2010. Permeant anions contribute to voltage dependence of ClC-2 chloride channel by interacting with the protopore gate. *J. Physiol.* 588:2545–2556. https://doi.org/10.1113/jphysiol.2010.189175

Sánchez-Rodríguez, J.E., J.A. De Santiago-Castillo, J.A. Contreras-Vite, P.G. Nieto-Delgado, A. Castro-Chong, and J. Arreola. 2012. Sequential interaction of chloride and proton ions with the fast gate steer the voltage-dependent gating in ClC-2 chloride channels. *J. Physiol.* 590:4239–4253. https://doi.org/10.1113/jphysiol.2012.232660

Schroeder, B.C., T. Cheng, Y.N. Jan, and L.Y. Jan. 2008. Expression cloning of TMEM16A as a calcium-activated chloride channel subunit. *Cell*. 134: 1019–1029. https://doi.org/10.1016/j.cell.2008.09.003

Segura-Covarrubias, G., I.A. Aréchiga-Figueroa, J.J. De Jesús-Pérez, A. Sánchez-Solano, P. Pérez-Cornejo, and J. Arreola. 2020. Voltage-dependent protonation of the calcium pocket enable activation of the calcium-activated chloride channel anoctamin-1 (TMEM16A). *Sci. Rep*. 10:6644. https://doi.org/10.1038/s41598-020-62860-9

Sheridan, J.T., E.N. Worthington, K. Yu, S.E. Gabriel, H.C. Hartzell, and R. Tarran. 2011. Characterization of the oligomeric structure of the Ca^{2+}-activated Cl^- Channel Ano1/TMEM16A*. *J. Biol. Chem.* 286:1381–1388. https://doi.org/10.1074/jbc.m110.174847

Terashima, H., A. Picollo, and A. Accardi. 2013. Purified TMEM16A is sufficient to form Ca^{2+}-activated Cl^- channels. *Proc. Natl. Acad. Sci. USA*. 110: 19354–19359. https://doi.org/10.1073/pnas.1312014110

Tien, J., C.J. Peters, X.M. Wong, T. Cheng, Y.N. Jan, L.Y. Jan, and H. Yang. 2014. A comprehensive search for calcium binding sites critical for TMEM16A calcium-activated chloride channel activity. *Elife*. 3:e02772. https://doi.org/10.7554/eLife.02772

Ullrich, F., S. Blin, K. Lazarow, T. Daubitz, J.P. von Kries, and T.J. Jentsch. 2019. Identification of TMEM206 proteins as pore of PAORAC/ASOR acid-sensitive chloride channels. *Elife*. 8:e49187. https://doi.org/10.7554/eLife.49187

Vaisey, G., A.N. Miller, and S.B. Long. 2016. Distinct regions that control ion selectivity and calcium-dependent activation in the bestrophin ion channel. *Proc. Natl. Acad. Sci. USA*. 113:E7399–E7408. https://doi.org/10.1073/pnas.1614688113

Wozniak, K.L., W.A. Phelps, M. Tembo, M.T. Lee, and A.E. Carlson. 2018. The TMEM16A channel mediates the fast polyspermy block in Xenopus laevis. *J. Gen. Physiol*. 150:1249–1259. https://doi.org/10.1085/jgp.201812071

Wright, E.M., and J.M. Diamond. 1977. Anion selectivity in biological systems. *Physiol. Rev*. 57:109–156. https://doi.org/10.1152/physrev.1977.57.1.109

Xiao, Q., K. Yu, P. Perez-Cornejo, Y. Cui, J. Arreola, and H.C. Hartzell. 2011. Voltage- and calcium-dependent gating of TMEM16A/Ano1 chloride channels are physically coupled by the first intracellular loop. *Proc. Natl. Acad. Sci. USA*. 108:8891–8896. https://doi.org/10.1073/pnas.1102147108

Yang, Y.D., H. Cho, J.Y. Koo, M.H. Tak, Y. Cho, W.-S. Shim, S.P. Park, J. Lee, B. Lee, B.-M. Kim, R. Raouf, Y.K. Shin, and U. Oh. 2008. TMEM16A confers receptor-activated calcium-dependent chloride conductance. *Nature*. 455:1210–1215. https://doi.org/10.1038/nature07313

Yu, K., C. Duran, Z. Qu, Y.Y. Cui, and H.C. Hartzell. 2012. Explaining calcium-dependent gating of anoctamin-1 chloride channels requires a revised topology. *Circ. Res.* 110:990–999. https://doi.org/10.1161/CIRCRESAHA.112.264440

Supplemental material

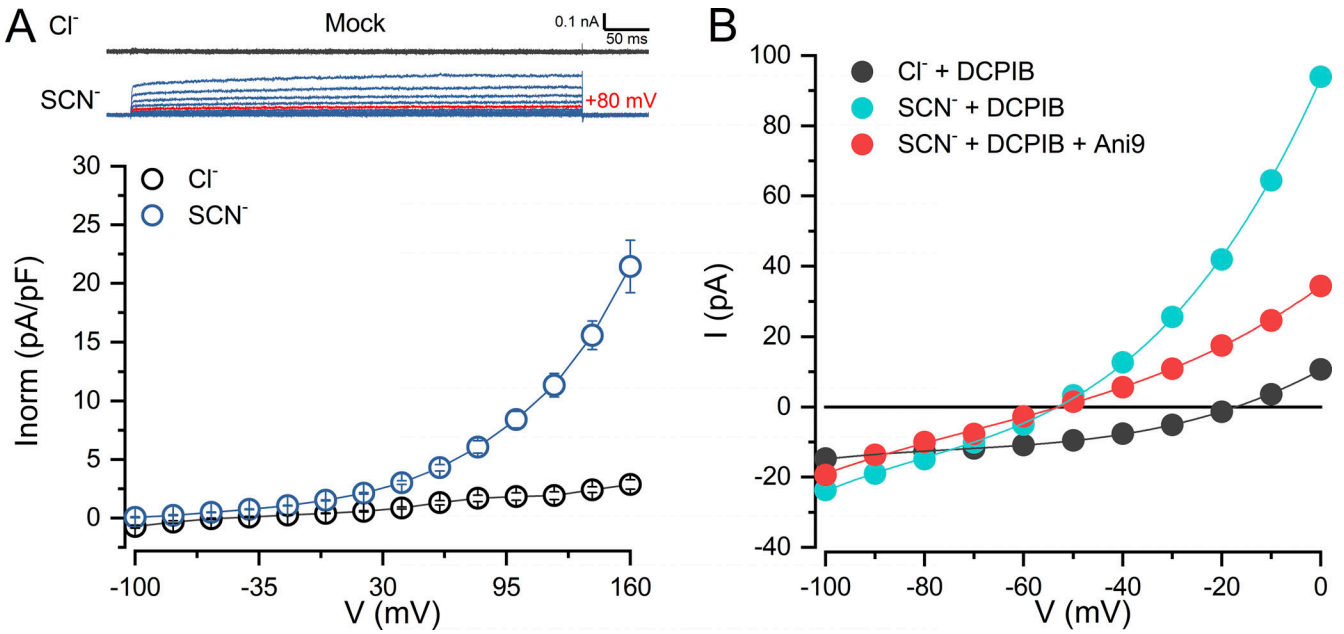

Figure S1. **HEK 293 cells transfected with the empty vector were voltage-clamped, and their membrane potential varied from −100 to +160 mV. (A)** The black traces were obtained from a cell bathed in a 140-mM Cl^- solution and dialyzed with a solution containing 40 mM Cl^-, 25 mM EGTA, and 0 Ca^{2+}. The blue traces are from a cell bathed in a 140 mM SCN^- medium and dialyzed with 40 mM Cl^-, 25 mM EGTA, and 0 Ca^{2+}. The red trace highlights the trace recorded at +80 mV to illustrate the current recorded at this potential in a whole cell. The lower panel shows the average I-V relations from cells bathed in Cl^- (black circles) or SCN^- (blue circles). **(B)** Example of I-V relations from a cell expressing the 5Q mutant channel bathed in Cl^- + 5 µM DCPIB (black), then SCN^- + 5 µM DCPIB (blue), and SCN^- + 5 µM DCPIB + 0.5 µM ANI9 (red). The cell was dialyzed with a solution containing 0 Ca^{2+} + 40 mM Cl^- and bathed in 140 mM Cl^-.

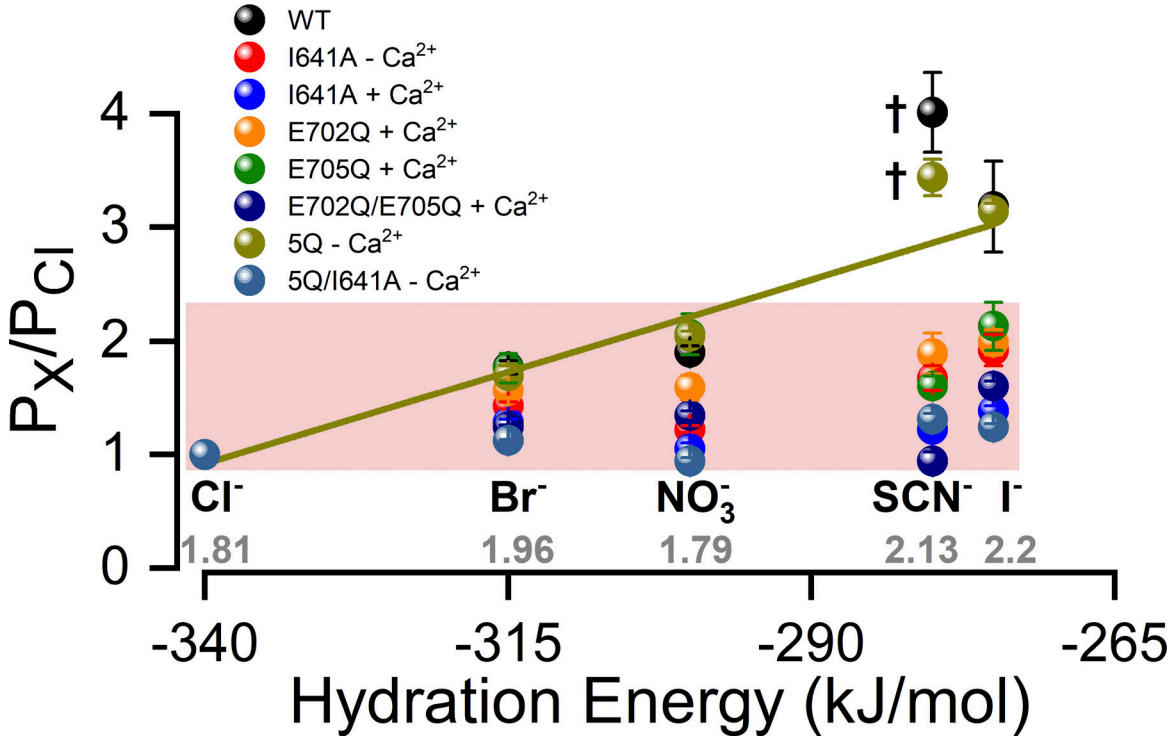

Figure S2. **Relationship between permeability ratio and anion hydration energy in TMEM16A channels.** Plotted values are the anion permeability ratios listed in Table 1 for the indicated channels. Hydration energy values are from Marcus (1997). In gray color, the radius of the anions (in Å) is indicated in gray. *t*, the SCN^- data was not included in the linear fit (continuous green line). The pink rectangle highlights the narrow range of permeability ratio values of the mutant channels.